Increasing Lateral-Directional Controllability and Investigating Elevator-Body Flap Interaction for Shuttle Orbiter

by

Connor Hoopes

A Thesis Presented in Partial Fulfillment
of the Requirements for the Degree
Master of Science

Approved April 2023 by the
Graduate Supervisory Committee.

Timothy Takahashi, Chair
Werner Dahm
Ruben Perez

ARIZONA STATE UNIVERSITY

May 2023

ABSTRACT

This thesis investigates the configurations needed to demonstrate positive lateral-directional controllability across the flight envelope of a hypersonic vehicle. It examines the NASA Space Shuttle Orbiter as a baseline reference configuration, as it was a successful hypersonic vehicle. However, the Orbiter had limited high-speed maneuvering capability; it relied on reaction-control jets to augment controllability due to a strong tendency for its aerodynamics to “control couple.” It was seen that many problems associated with the control of the hypersonic Orbiter are due to its slender configuration. This work relies upon the Evolved-Bihrle-Weissman chart as an accurate indicator of lateral-directional stability and controllability. The also explores variant configurations of larger wing tip verticals to explore what configuration changes are needed to reduce dependence on reaction controls.

ACKNOWLEDGEMNT

This work would like to acknowledge that it is a direct result of and inspired by the prior work, “Hypersonic Aircraft Performance Limitations Arising from Aerodynamic Control Limits” conducted Giffin and Takahashi. While the prior work was completed and supported in part by the Postgraduate Research Participation Program at the U.S. Air Force Institute of Technology, administered by the Oak Ridge Institute for Science and Education through an interagency agreement between the U.S. Department of Energy and AFIT, this work was solely conducted via Arizona State University and was not funded by the U.S. AFIT program.

TABLE OF CONTENTS

Page

Page

LIST OF TABLES

Table Page

LIST OF FIGURES

Figure Page

Figure Page

Figure Page

Figure Page

Figure Page

Figure Page

INTRODUCTION

The development of a truly general purpose, air-breathing maneuvering hypersonic flight vehicle has largely eluded the aerospace community. On one hand we have recent limited maneuverability air-breathing hypersonic propulsion testbeds like the NASA Hyper-X [1] and Air Force X-51 [2] on the other hand, we have the broadly maneuvering integral-rocket propelled NASA/Air Force/North American X-15 [3] from the 1960's. Also in the mix is the NASA/Rockwell Space Shuttle orbiter, which is "flown" as a glider during reentry with significant down-range and cross-range maneuvering performance. Little publicly released data exists detailing the aerodynamic stability of Hyper-X and X-51; while considerable detailed data exists for both the X-15 and the Orbiter [4][5].

Both the X-15 and Orbiter have successfully flown large numbers of missions spanning both the hypersonic and the subsonic flight regimes. The X-15 reached a top speed of Mach 6.7 at an altitude of 354,000 feet [6]. Extremely high-speed flight presents numerous design challenges. The Space Shuttle Orbiter successfully flew many missions spanning both the hypersonic, supersonic and the subsonic flight regimes; the Shuttle orbiter reached speeds in excess of Mach 25 on reentry. The "hypersonic" regime unequivocally encompasses operations above Mach 5; but the distinction between supersonic and hypersonic is not always clear. Above Mach 3 and below Mach 8, where air dissociates into a plasma, exists a region where classical design principles like "simple sweep theory" and "slender body theory" no longer apply but flow remains amenable to be analyzed using linear potential flow codes.

Above these speeds, “real gas effects” became significant as the flow around the Orbiter would partially dissociate, enveloping it in a plasma [7][8]. The flight conditions and flight dynamics problems discussed in the paper will be restricted to flight conditions where “real gas effects” are not significant.

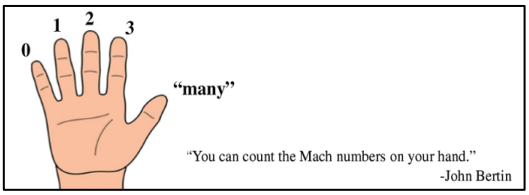

FIGURE 1. Hypersonic Flight Issues [8].

Since both the X-15 and the Shuttle Orbiter operate over a wide range of speeds, we must understand how their respective aerodynamic properties vary widely across their flight envelopes. [8] As the freestream Mach numbers increase from subsonic to hypersonic, the source of lift changes from being leeward surface dominated (upper surface “suction side”) to windward surface dominated (lower surface “impact pressure side”). This results in strong changes in fundamental vehicle level aerodynamic properties at increased Mach numbers; see FIGURE 1.

A general-purpose flight vehicle must demonstrate positive stability and controllability over a range of speeds, altitudes, and weights. From a flight control perspective, positive stability means a tendency to respond to disturbances through damped oscillations about a baseline state. Positive vehicle stability may be obtained by 1) inherent aerodynamic static stability or 2) through some form of active closed-loop control or 3) through a combination of both. Controllability means that the pilot, or autopilot, can direct changes in vehicle speed, altitude, and heading which the

vehicle will follow. Satisfactory controllability requires both sufficient authority, (the ability to generate forces and moments) and frequency bandwidth (the ability for the vehicle to follow a close succession of differing commands).

Classic aircraft design considers longitudinal (pitch-plane) stability and controllability to be fundamentally decoupled from lateral-directional (roll-yaw-plane) stability and controllability. However, real aircraft tend to exhibit some level of coupling between pitch and roll-yaw dynamics. Hypersonic vehicles, such as the Orbiter, tend to be long and slender; they have inherent mass properties that accentuate cross-coupling [9]. As flight speeds increase, the windward surface dominated aerodynamics also accentuate cross-coupling due to degraded inherent static directional stability trends. High Mach numbers also reduce all forms available aerodynamic control power. Taken together, the configurator of the aerodynamic shape of a hypersonic vehicle must carefully consider the implication of the proposed loft on the "quantity" and "quality" of the basic aerodynamic stability, terms like $dCm/d\alpha$, $dCn/d\beta$, and $dCl/d\beta$. The "quantity" of aerodynamic control power are terms like *dCm/delevator*, *dCn/drudder*, or *dCl/daileron*. The "quality" of aerodynamic control power is the magnitude of un-intended byproducts of control surface movement, things like static directional stability changes due to elevator deflection, or adverse-yaw-due-to-roll from the ailerons, or even adverse-roll-due-to-yaw from the rudder.

Recent work at Arizona State University (ASU) [10][11][12][13] has highlighted how important aerodynamic control-coupling metrics developed to support transonic maneuvering fighter aircraft are to screen candidate hypersonic and other high-speed configurations. For lateral-directional stability "quantity" and control "quality," a diagram known as the Bihrle-Weissman Chart proves to be an effective indicator of hypersonic flying qualities [14]. For example, the USAF/NASA/North American X-15 proves to have inherently favorable flying characteristics according to Bihrle-Weissman criteria; and indeed, pilots flew over two hundred successful missions. Provided the X-15 was flown within the atmosphere (i.e., at reasonable dynamic pressure) its inherent aerodynamic stability and controllability was sufficient for controlled maneuvering flight. Only when flown at the outer reaches of the atmosphere, at low dynamic pressure, did it require reaction-jet thrusters to command attitude.

Conversely, the ASU team noted that the Shuttle Orbiter needed to use its reaction control system (RCS) thrusters deep into atmosphere at speeds as low as Mach 1, mere minutes before touchdown; see FIGURE 2.

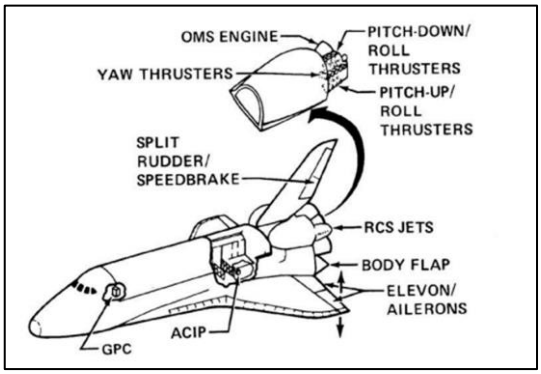

FIGURE 2. Shuttle configuration [17].

A NASA flight test report noted that "stability augmentation is provided by the aft reaction control system (RCS) jets… The aft yaw jets are active until Mach 1, while the pitch and roll jets are terminated at a pressure of 20 and 10 pounds per square foot, respectively." [15] Thus, we realized that a configuration like the X-15 has nearly semi unlimited hypersonic maneuvering capability while the Shuttle Orbiter's atmospheric maneuvering capability is limited by the propellant load feeding and size of the thrusters of its RCS system [16][17]. Circumstantial evidence, that the Shuttle was never flown on polar orbit missions, which would require substantial maneuvering to align with the re-entry and landing approach profiles despite ostensibly being designed to fly them, suggests that the need for active RCS augmentation at all supersonic speeds substantially limited its endo-atmospheric hypersonic performance.

Thesis

This thesis will analyze the baseline Shuttle Orbiter to understand its aerodynamic stability and develop alternative configurations that will improve its open-loop stability. It will investigate the shuttle's lateral-directional stability and demonstrate that longitudinal maneuvers can impact the lateral-directional stability.

WHAT IS A WEISSMAN CHART?

Aircraft designers seek rapid methods to screen candidate configurations for inherently favorable or unfavorable flying qualities. The "Weissman Chart" proves to be a durable metric; it was proposed in 1972 by Robert Weissman in an M.S. Thesis at the University of Dayton [18]. "Weissman developed this criterion from analyzing time history sensitivity studies to lateral/directional static stability derivatives in a digital six degree-of-freedom off-line simulation. Based on these time history traces Weissman empirically identified regions of increasing roll departure severity and spin susceptibility." [18] The chart along with its regions is shown in FIGURE 3.

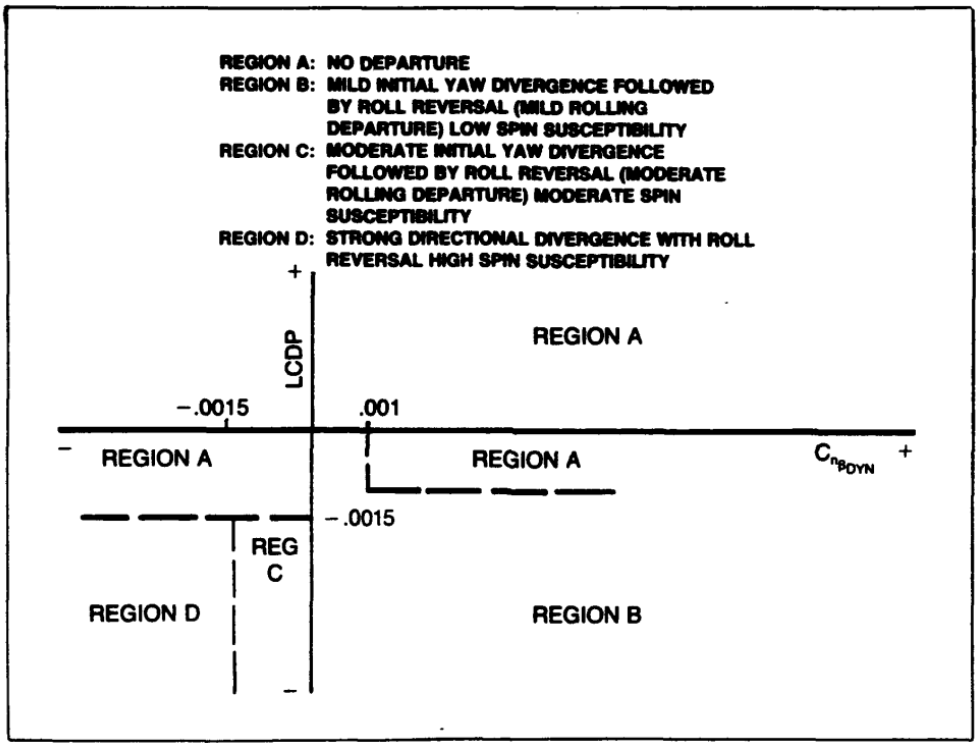

FIGURE 3. Weissman Chart [18].

The two axis that are used in the chart represent $Cn_{\beta DYN}$ and *LCDP*. $Cn_{\beta DYN}$ is the Dutch-Roll Stability parameter (yawing moment coefficient with respect to side slip adjusted for vehicle mass properties) and the *LCDP* is the Lateral Control Departure Parameter, a metric of the "quality" of the aileron effect of the lateral control surfaces [19][20][21][22].

$$Cn_{\beta DYN} = \frac{dCn}{d\beta} * cos(\alpha) - \frac{dCl}{d\,\beta}\left(\frac{I_{zz}}{I_{xx}}\right) * sin(\alpha) \quad (1)$$

$$LCDP = \frac{dCn}{d\beta} - \frac{dCl}{d\beta} * \frac{\frac{dCn}{d\ aileron}}{\frac{dCl}{d\ aileron}} \quad (2)$$

In a paper to be published in the 2023 AIAA Aviation Conference, Takahashi, Griffin & Grandhi present an evolved version of this chart; refer to FIGURE 4. [23] Their work builds on earlier efforts by Bihrle, Skow [24] and Mason [14] among others, and has been tailored to address challenges of slender, high-speed vehicles. Based on both Skow's [24] experience with the Northrop T-38/F-5 and their own review of observed flying qualities deficiencies of the Bell X-2, they moved the boundary of the "F" to "A" region to require additional open loop Dutch Roll stability to guarantee "Highly Departure and Spin Resistant Flight." Ideally, a general-purpose maneuvering vehicle will need to have its "open-loop" aerodynamics firmly planted in region "A" of the Evolved-Bihrle-Weissman Chart.

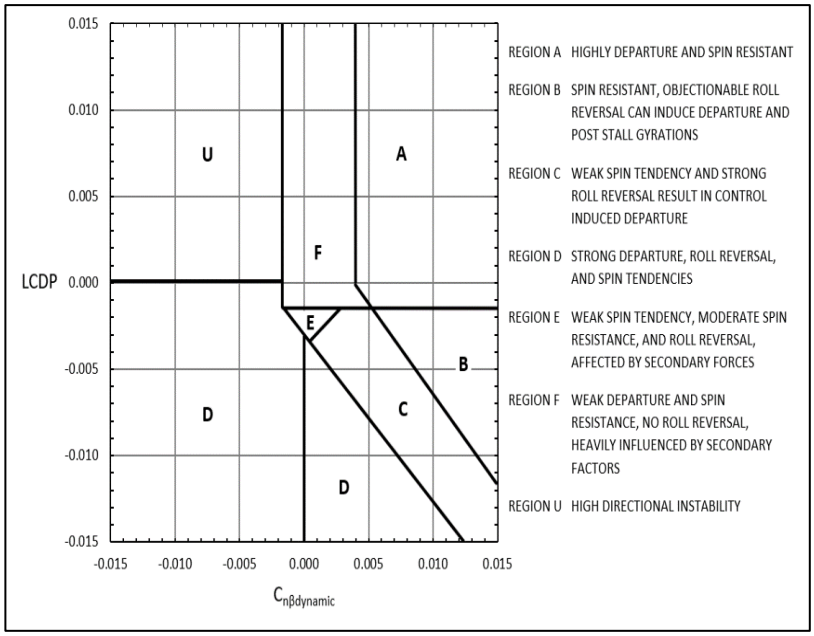

FIGURE 4. Evolved Bihrle-Weissman Chart after Takahashi, Griffin & Grandhi [23].

Aircraft have no inherent desire to stay right-side up as their aerodynamics are usually capable of overwhelming whatever "pendulum stability" they may possess. Thus, to maintain nominally "straight-and-level" flight, aircraft must be locked into a stable oscillatory "Dutch-Roll" mode where they gently rock back and forth in a combined rolling and yawing motion [21][25][26][27].

Directional stability must be maintained for an aircraft to be stable in forward flight otherwise they will diverge in course heading. Since aircraft must weathercock into the wind, rather than depart, they must display $dCn/d\beta > 0$ whether by inherent aerodynamic effects or through closed loop control. Typical low speed aircraft have large tails and develop weathercock stability entirely through passive aerodynamic

effects. Other vehicles, such as rockets or stealth aircraft, may utilize a closed-loop feedback control system using either active rudder control, active laterally disposed drag brake control and/or vectored thrust to develop their synthetic stability. We will see later in this paper that the X-15 had inherent static directional stability while under many conditions, the Space Shuttle Orbiter lacked inherent aerodynamic stability and relied upon reaction control jets (RCS) to keep its nose pointed forwards [13][28].

Aerodynamic lateral stability is commonly associated with the effects of positive effective dihedral. Thus, to be stable laterally, the aircraft must develop a rolling moment to oppose sideslip*:* $dCl/d\beta < 0$ whether by inherent aerodynamic effects or through closed loop control.

All factors taken together, the aircraft designer must be vigilant so that the proposed vehicle is not directionally divergent, never expresses unstable Dutch Roll, does not exhibit Control Coupling which leads to an inadvertent spin, and avoids negative damping associated with Inertial Coupling [21][22]. The Dutch Roll mode is the easiest to assess. Recall that it is a combined lateral-directional motion [21]. At first order, we may estimate it by:

$$\omega_{dr} = \frac{1}{2\pi}\sqrt{\frac{57.3*Cn_{\beta DYN}*q*S_{ref}*b}{Izz}} \quad (3)$$

Thus, an oscillatory Dutch Roll Frequency exists proportional to the square root of $Cn_{\beta DYN}$, provided that, it is positive. The frequency also scales proportional to the square root of the dynamic pressure and inversely proportional to the square root of the mass-moment-of-inertia in yaw. MIL-STD 8785C [28] and MIL-STD 1797A [30] provide guidelines to the preferred frequency range for the Dutch Roll. MIL-STD 8785C recommends minimum Dutch Roll Frequencies for design; it should not be so slow to lead to phase-lag when the pilot (or autopilot) commands maneuvers. While MIL-8785C has no upper bound, it should not be so fast as to provoke structural resonance [21]. However, as the frequency increases, the aircraft will become more responsive to roll inputs.

If $Cn_{\beta DYN}$ is negative, the Dutch Roll frequency becomes an imaginary number, i.e., it is divergent and indicates an inherent tendency for the vehicle to go out of control. There are several ways $Cn_{\beta DYN}$ can be negative; the Dutch Roll mode can be unstable where despite positive static directional stability, the aircraft experiences overall lateral-directional instability; this is when $dCl/d\beta > 0$ and overwhelms the stabilizing contributions of $dCn/d\beta > 0$. On the flip side, an aircraft that lacks static directional stability can have overall lateral-directional stability provided it has enough effective dihedral; this exists only when $dCl/d\beta << 0$. Since static directional stability ($dCn/d\beta$) declines with increasing Mach number, many designers of high-speed vehicles (including those who configured the Space Shuttle Orbiter) exploit the very strong effective dihedral of a highly swept wing flown at high angles of attack to get positive $Cn_{\beta DYN}$ despite poor static directional stability.

The Space Shuttle Orbiter conceptual designers may have overlooked the magnitude of the problem associated with Control Coupling while prioritizing other features. This is the factor associated with *LCDP*. Control coupling occurs when static yaw and roll stability interact with the moments from control surfaces in a manner that is destabilizing. Pilots can no longer trim their aircraft in yaw and roll. They also describe situations where the 'controls reverse'.

Recall that Weissman realized that *LCDP* was critical to inherent flying characteristics. Since $LCDP = \frac{dCn}{d\beta} - \frac{dCl}{d\beta} * \frac{\frac{dCn}{d\,aileron}}{\frac{dCl}{d\,aileron}}$ and it needs to be positive, a vehicle needs to have sufficient stick-fixed directional stability ($dCn/d\beta > 0$) to balance the remainder of the right-hand-side of the equation. Because $dCl/d\beta < 0$ for slender swept-configurations at positive-angle-of-attack, the sign of the yaw-to-roll-ratio of the "aileron" controls is critical determining whether *LCDP* is positive or negative. A slender, swept vehicle with unfavorable "adverse yaw" from its "ailerons" tends to negative *LCDP*. When an aircraft has adverse aileron control where, in the absence of pilot applying opposing rudder, roll command inputs will destabilize the aircraft in yaw.

LCDP, as applied to the Bihrle-Weissman chart, may represent either the "open-loop" or a "closed-loop" performance of the "ailerons." On a typical aircraft, designers implement "Aileron-Rudder-Interconnect" to automatically apply some rudder in conjunction with aileron to reduce (or eliminate) adverse yaw. If adverse yaw

were to be eliminated, LCDP ~ $dCn/dbeta$; which so long as $dCn/dbeta$ > +0.004 would place the vehicle in region "A" of the Bihrle-Weissman chart. Aileron-Rudder-Interconnect is a form of "feed-forward" control augmentation that reflects the "closed-loop" performance of the aircraft. For the Shuttle Orbiter, the "open loop" LCDP represents the totality of usable aerodynamic control; ARI is not a viable control law. This is because the split-rudder is rarely used as a yaw control device; at supersonic speeds it is fully open in "speed brake" mode to help augment static directional stability and at subsonic speeds it is used to modulate drag to assist in speed control. Substantial classical rudder control is only usable moments before a cross wind touchdown. As such, the only remaining control device to counteract the adverse yaw of the ailerons (and improve LCDP) are the lateral reaction control system (RCS) hydrazine jets.

X-15 SUMMARY

The USAF/NASA/North American X-15 flew over two hundred research missions; including captive carry, gliding and powered operations. X-15 flights set enduring speed and altitude records, including 4 flights over Mach 6 and 13 flights at altitudes in excess of 50 miles. When the X-15 was flown within the atmosphere, at reasonable dynamic pressures, it had sufficient inherent aerodynamic stability and controllability to perform significant maneuvers [3].

FIGURE 5. North American X-15.

In general, the X-15 had solid aerodynamic stability and control. The aircraft had positive directional stability at all speeds and attitudes; it also had a stable Dutch Roll mode at all times; pilot comments were all favorable [28]. At high true airspeed, aerodynamic damping would diminish; making the use of a "stability augmentation system" to provide synthetic damping desirable. On Flight 191, where that system failed in a manner where it destabilized the aircraft, the aircraft lost control, overstressed its structure and disintegrated mid-air killing pilot Michael Adams [4]. At very high altitudes, where dynamic pressure fell below 100-KEAS and the resulting stick-fixed frequencies became objectionably slow, pilots would transition to reaction-jet thrusters to command attitude, roll and sideslip [4].

FIGURE 6 reiterates the Weissman Chart for the X-15, as generated by Griffin & Takahashi [14]. Plotting the entire database from low speed to high speed and from low angles of attack through high angles of attack, we can see that the airframe is firmly placed in the "A" region. For the X-15 *LCDP* was favorable for three reasons: first the airframe has unusually large vertical tail surfaces (see FIGURE 5) and secondly, the X-15 has only moderate wing sweep (also see FIGURE 5), and finally, that the X-15 "aileron" control comes from differential deflection of the horizontal tail surfaces rather than from wing mounted physical ailerons. Thus, *LCDP* remains positive due to the strong positive $dCn/d\beta$ not being overwhelmed by a large negative $dCl/d\beta$ multiplying a large adverse yaw term.

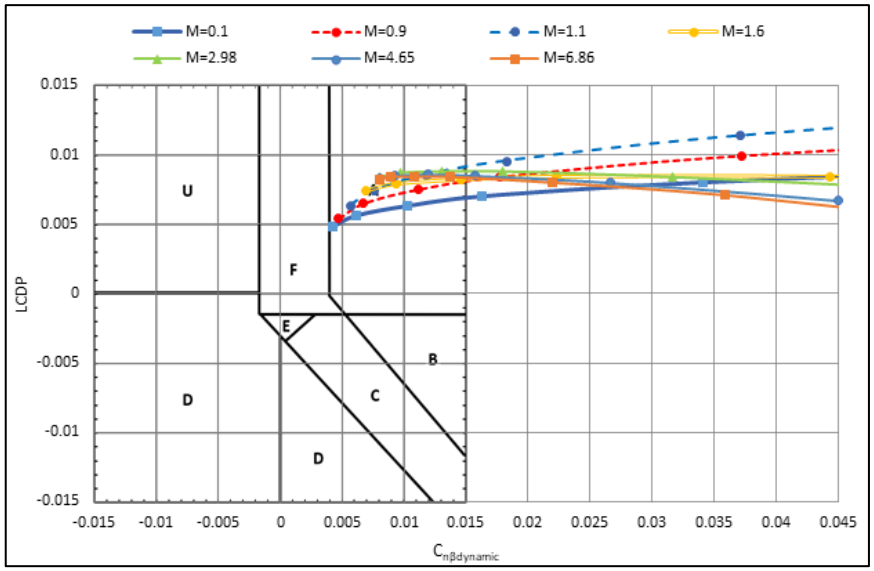

FIGURE 6. Evolved Bihrle-Weissman Chart for the X-15 [13].

BASIC APPROACH TO ANALYZE THE SHUTTLE ORBITER

Our Space Shuttle Orbiter approach considers both the baseline Orbiter, as fielded in gliding drop tests and on 135 orbital missions and proposed variants of the Orbiter designed to have improved gliding maneuverability obviating the need for RCS jets to be used deep in the atmosphere.

For the baseline Orbiter, we approach the problem from two directions: first, to plot flight-test reduced data onto the Bihrle-Weissman chart and second, to develop general aerodynamic databases to examine the stability and controllability of the Orbiter over a broader flight envelope than it experienced in operation. For the proposed aerodynamic variants, we must rely solely on estimated aerodynamic data. In this paper, we will use VORLAX for the computational methods to estimate the aerodynamic data.

Flight Test

Flight Test data has been extracted from a number of papers published by NASA/Langley arising from a 1983 “Lessons Learned” conference [5]. We source much of our comparison data from a paper given at that conference titled “Stability and Control Over the Supersonic and Hypersonic Speed Range.” [31] This source provided the rolling moment and yawing moment charts used for the Bihrle-Weissman chart analysis and is the baseline for the comparison to the models for accuracy and model validity. We also rely on other sources for general background information regarding Shuttle Orbiter nominal re-entry trajectories as well as the final approach and landing [7][32][33][34][35][36]. With the availability of very detailed flight histories, we reconstructed a trajectory with known control surface commands. See TABLE 1 and Appendix A. for the charts used to reconstruct the trajectory table.

TABLE 1. Reconstructed Flight Data

Mach	Alpha	Elevon	BodyFlap	SplitFlap	L/D	CL	CD	CnB	ClB	Cnda	Clda
2	12	5	-4			0.4	0.2	-0.0008	-0.0015	-0.0002	0.001
4	20	5	4	75	1.8077	0.42	0.25	-0.0017	-0.0016	-0.0003	0.000
6	27	3.25	6	85	1.5349	0.51	0.31	-0.0018	-0.0017	-0.0004	0.001
8	34	2.5	8	85	1.295	0.72	0.52	-0.0015	-0.0021	-0.0004	0.001
10	39	1	8	85	1.1012	0.851	0.8	-0.0016	-0.002	-0.0005	0.001
12	40	1	8	0	1.0745	0.9	0.9	-0.0016	-0.0021	-0.0005	0.001
14	40	1	8	0	1.0745	0.9	0.85	-0.0016	-0.0021	-0.0005	0.001
16	40	1	8	0	1.0745	0.9	0.85	-0.0016	-0.0021	-0.0005	0.001
18	40	1	8	0	1.0745	0.85	0.79	-0.0016	-0.0021	-0.0006	0.001
20	40	1	8	0	1.0745	0.85	0.79	-0.0016	-0.0021	-0.0006	0.001
22	40	1	8	0	1.0745	0.85	0.8	-0.0016	-0.0021	-0.0006	0.001
24	40	1	8	0	1.0745	0.85	0.76	-0.0016	-0.0021	-0.0008	0.002
26	40	1	8	0	1.0745	0.85	0.76	-0.0016	-0.0021	-0.0009	0.002

VORLAX

VORLAX is a vortex lattice potential flow solving panel-method Computational Fluid Dynamics (CFD) code written in FORTRAN [37][38]. It can be used to determine lift, inviscid drag, and the stability derivatives of arbitrary configurations. It has both subsonic and supersonic leading edge flow models. The supersonic leading-edge flow model accounts for shock waves developed at the leading and trailing edges; as such it is valid for "slender" shapes that do not develop off-body standing shock waves. VORLAX solutions fundamentally neglect thickness effects, and as such will under-predict the directional stabilizing effect of the Orbiter's split-wedge "speed brake" rudder. It also cannot capture any sort of "real-gas-effects" of high temperature air. Despite these limitations, Griffin & Takahashi showed that it worked remarkably well to estimate the aerodynamic stability of the X-15 up through Mach 6 [13].

To make a VORLAX input file, general dimensions of the vehicle are found from a reputable source and reduced in a simple line geometry. This is shown in FIGURE 7 and FIGURE 8. Shuttle geometry is taken in from FIGURE 7 and then, in FIGURE 8 the basic shape is remade as a collection of flat panels. VORLAX has the capability to represent control surfaces, vertical tails, and other characteristics such as dihedral and wing sweep. It can then run through various Mach numbers and angles of attack while also incorporating sideslip. VORLAX results are in the wind/stability axis. Therefore, simple transformations are necessary to convert from wind to body axis when comparing to flight data or wind tunnel data. See Appendix B for VORLAX input files.

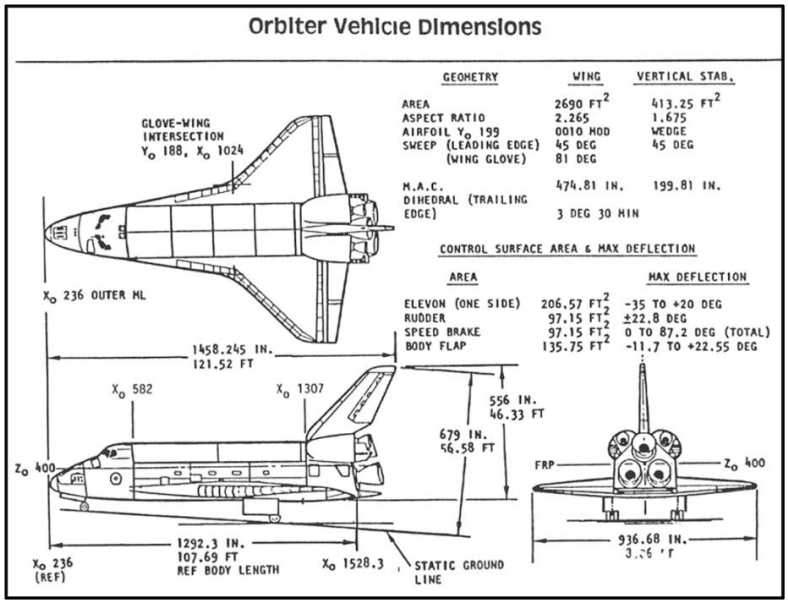

FIGURE 7. Orbiter Shuttle Dimensions [39].

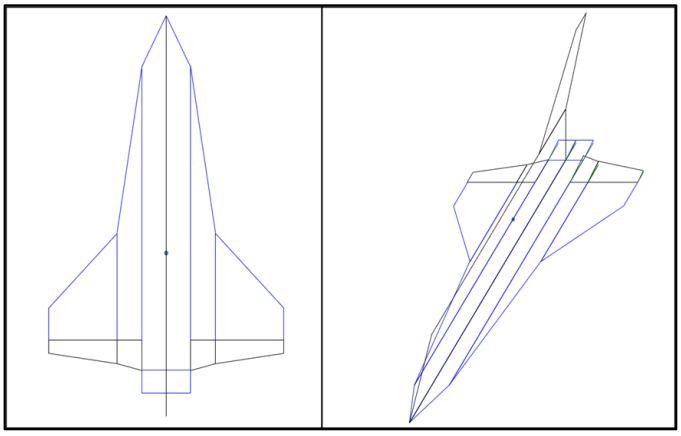
FIGURE 8. VORLAX Panels.

In this section, we will use it to estimate the aerodynamic stability of the Orbiter at speeds below Mach 3. This thesis also compares VORLAX to flight test data for the Space Shuttle Orbiter at speeds up to Mach 6. A full set of computational aerodynamic data points could be developed and used in the validation of the baseline model. With the baseline computational aerodynamic model validated, comparison to the Bihrle-Weissman Chart could be made and other variations could be analyzed.

Screening Plots and Stability Recap

For the analysis of the baseline shuttle and the possible variants via the flight test data or the computational aerodynamic database, screening plots are used to assess the stability of the configuration. The plots help to understand the vehicle response due to changes in Mach number, angle of attack (α), sideslip (β), or control surface deflection. They further help to illustrate the longitudinal and lateral-directional stability. See FIGURE 9 for typical plots, FIGURE 10 for longitudinal plots, and FIGURE 11 for the lateral-directional plots.

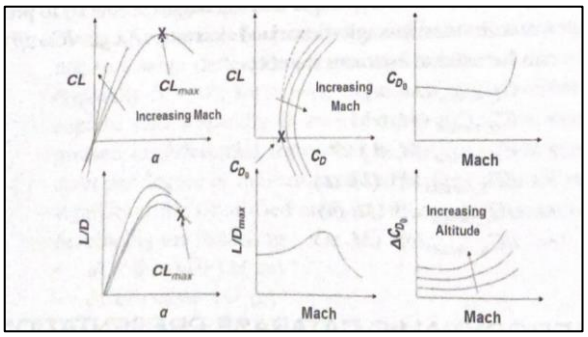

FIGURE 9. Typical Screening Plots [21].

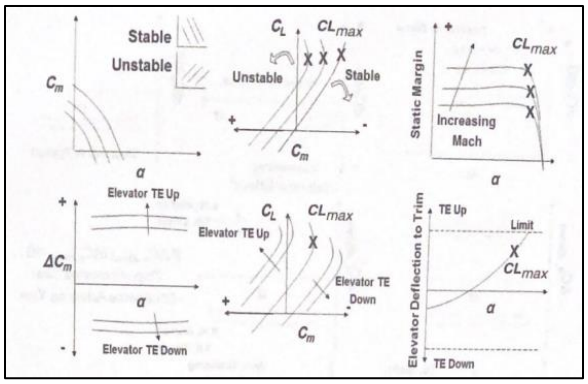

FIGURE 10. Longitudinal Screening Plots [21].

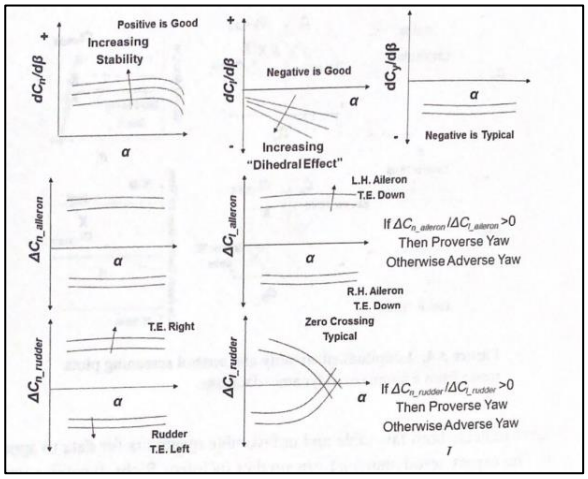

FIGURE 11. Lateral-Directional Screening Plots [21].

For the purposes of this paper, lift coefficient (C_L) versus angle of attack (α) will be utilized due to VORLAX limitation for thickness. VORLAX can do thickness via its "sandwich panels" method but was not utilized for this and beyond the scope of this analysis. It is well understood and seen in FIGURE 9 that the coefficient of lift (C_L) versus angle of attack (α) should be typically linear. It should increase proportionally to increases in angle of attack. It also increases with Mach number increases as well. This will be important in the subsequent screening plots. The axis system for the aircraft is shown again in FIGURE 12.

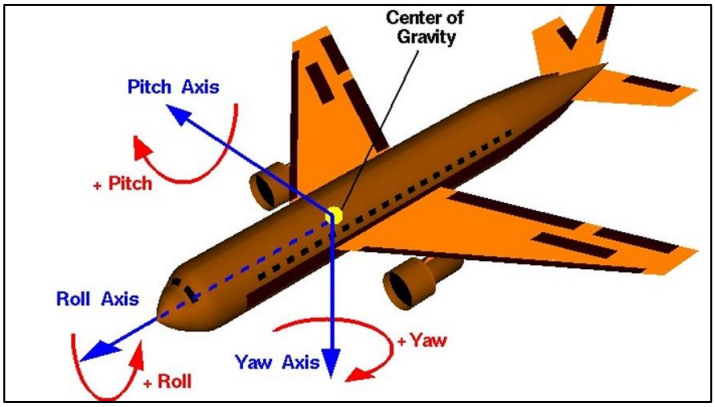

FIGURE 12. Typical Aircraft Axis [40].

For longitudinal stability in FIGURE 10, two plots will be used primarily, those being the pitching moment (C_m) versus angle of attack (α) and the lift coefficient (C_L) versus pitching moment (C_m). These two plots are important in the vehicle's stability. As seen in the aircraft axis FIGURE 12, positive pitching moment (C_m) would correspond to positive angles of attack (α), therefore, to maintain a stabilizing nose down motion, you would want a decreasing pitching moment (C_m) versus increasing angle of attack (α). This is shown in FIGURE 10. Likewise, because lift coefficient (C_L) can increase with increases in Mach number and angle of attack as seen in FIGURE 9, a comparison of lift coefficient (C_L) to pitching moment (C_m) would be important to capture any variance in maneuvers and their impact on the longitudinal stability.

For the lateral-directional screening, two plots will be used as the primary indicators. Those being the yawing moment due to sideslip ($dC_n/d\beta$) versus angle of attack (α) and rolling moment due to sideslip ($dC_l/d\beta$) versus angle of attack (α). Yawing moment axis (C_n) as seen in FIGURE 12 shows that it is positive and moving from port to starboard. If the aircraft is flying at sideslip (β), then it would be desirable for the aircraft to yaw positively to regain nose straight. This is shown in FIGURE 11 that for yawing moment due to sideslip ($dC_n/d\beta$) versus angle of attack (α). Similarly for rolling moment due to sideslip ($dC_l/d\beta$), because rolling moment is defined as positive from port to starboard rolling over the top of the vehicle, it would be good to have a negative rolling moment due to sideslip ($dC_l/d\beta$). This would mean that as the aircraft is flying at sideslip, or crabbed into the wind, that for changes in angle of attack

(α) the vehicle would not continue an exacerbating roll but maintain a wing downward motion and level out motion.

BASELINE SHUTTLE LATERAL-DIRECTIONAL CONTROLLABILITY

In order to find the baseline *LCDP* and $Cn_{\beta DYN}$ values four key values were necessary, those being Cl_{β}, $C_{n\beta}$, C_{lda}, and C_{nda}. Through the equations (1) and (2), the results can be plotted on the Evolved-Bihrle-Weissman Chart.

The flight data that was utilized can be seen FIGURES 13. through 16. They provided the Cl_{β}, $C_{n\beta}$, $C_{l\gamma a}$, and $C_{n\gamma a}$ all per deg and through the shuttles entire flight regime; shuttle reports present the data in BODY AXIS. That being the hypersonic region all the way down to subsonic region. In order to back out the necessary values from the "per deg" values present in the charts to the values needed for the *LCDP* calculations, specific Mach numbers would need to be selected and that control point's corresponding Angle of Attack could be used. See FIGURE 17 for the angle of attack schedule [17].

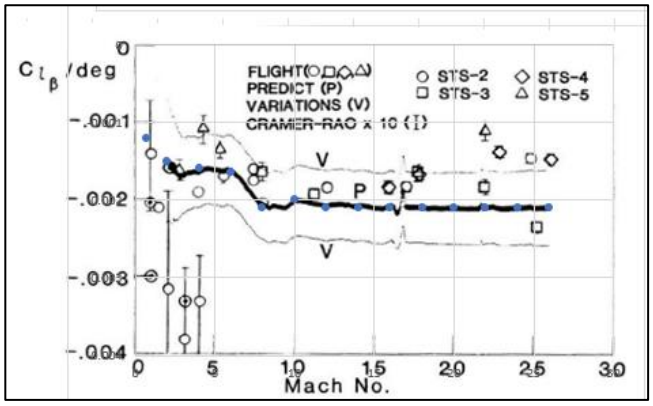

FIGURE 13. Shuttle Flight Test $dC_l/d\beta$ [31].

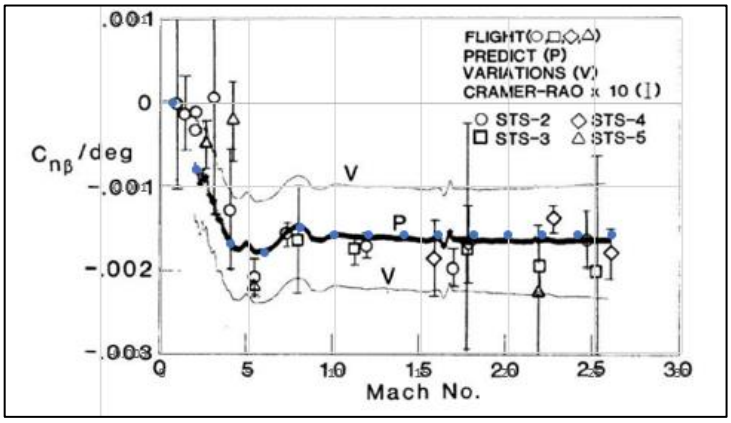

FIGURE 14. Shuttle Flight Test $dC_n/d\beta$ [31].

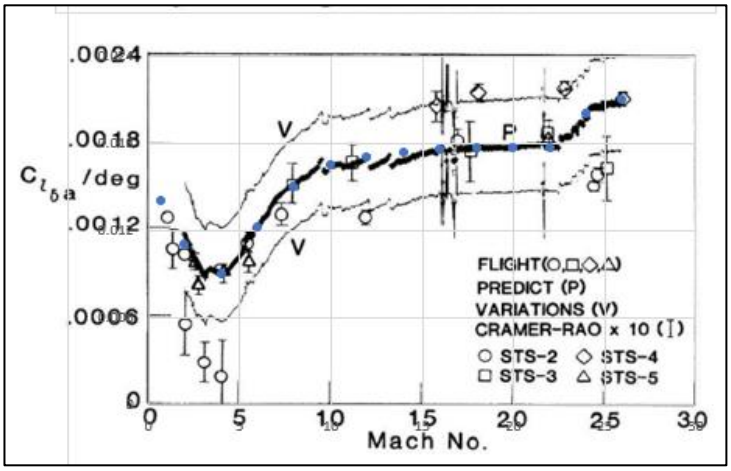

FIGURE 15. Shuttle Flight Test $dC_l/dail$ [31].

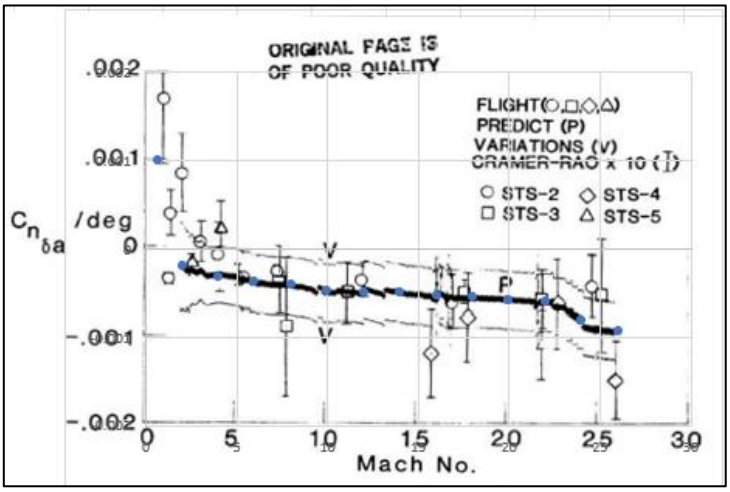

FIGURE 16. Shuttle Flight Test $dC_n/dail$ [31].

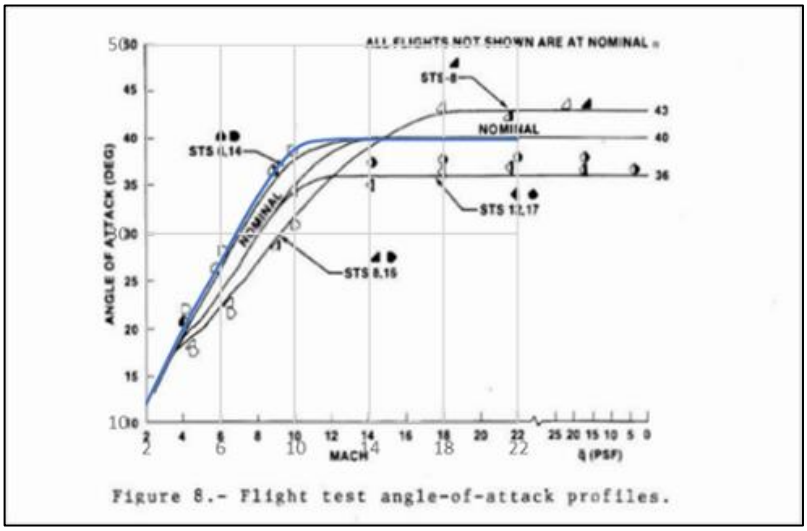

FIGURE 17. Mach Number vs Angle of Attack.

The $Cn_{\beta DYN}$ is reliant on the ratio of the Mass Moments of Inertia. For the calculations. The value for the Izz/Ixx = 8.01. This is taken from STS-1 [31] [36]. With the angle of attack schedule (FIGURE 17), and the yaw-rolling moment charts (FIGURE 13. thru FIGURE 16), we tabulated the values were tabulated and calculated to find the *LCDP* and $Cn_{\beta DYN}$. The tabulated values for the given control points are shown in Table 2. The Evolved-Bihrle-Weissman Chart for the baseline shuttle could then be presented from the tabulated values from the flight test data; see FIGURE 11. The results are presented in the body axis coordinate system. See FIGURE 18 for shuttle axis. It Matches typically aircraft axis seen in FIGURE 12.

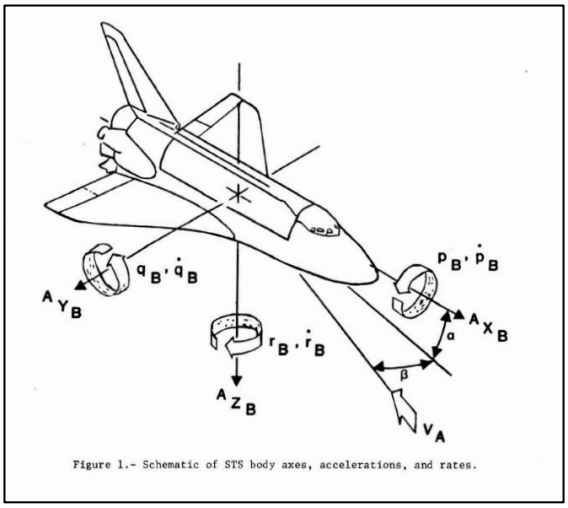

FIGURE 18. Shuttle Axis System [31].

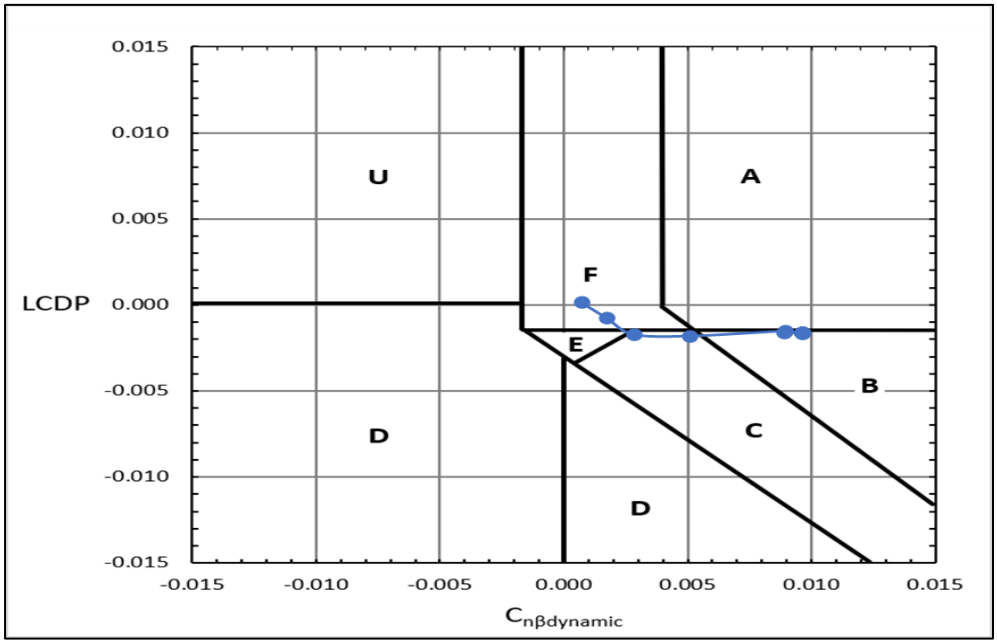

REGION A	HIGHLY DEPARTURE AND SPIN RESISTANT
REGION B	SPIN RESISTANT, OBJECTIONABLE ROLL REVERSAL CAN INDUCE DEPARTURE AND POST STALL GYRATIONS
REGION C	WEAK SPIN TENDENCY AND STRONG ROLL REVERSAL RESULT IN CONTROL INDUCED DEPARTURE
REGION D	STRONG DEPARTURE, ROLL REVERSAL, AND SPIN TENDENCIES
REGION E	WEAK SPIN TENDENCY, MODERATE SPIN RESISTANCE, AND ROLL REVERSAL, AFFECTED BY SECONDARY FORCES
REGION F	WEAK DEPARTURE AND SPIN RESISTANCE, NO ROLL REVERSAL, HEAVILY INFLUENCED BY SECONDARY FACTORS

FIGURE 19. Evolved-Bihrle-Weissman Chart based on Shuttle Flight Test.

Examining FIGURE 19, the Evolved-Bihrle-Weissman Chart for the Space Shuttle Orbiter, we see the following trends on re-entry. At the highest Mach numbers, early during re-entry where dynamic pressure is low and the Orbiter is flown far nose-up its performance straddles the line between the stable region "A" and the unstable regions "B" and "C." While $Cn_{\beta DYN}$ is strongly positive, *LCDP* is nearly zero; clearly closed-loop RCS control is needed here. The Bihrle-Weissman chart presumes that longitudinal and lateral-directional dynamics are fully decoupled. Looking at FIGURE 20, the reader may see that the Orbiter operates over a very wide range of angles of attack during re-entry, approach, and landing. However, the angle of attack does not change very quickly. Although the Orbiter is a maneuvering Hypersonic vehicle, it has low bandwidth requirements in terms of commanded pitch rate.

TABLE 2. Table of values and calculations for *LCDP* and $Cn_{\beta DYN}$

Mach	**0.7**	**2**	**4**	**6**	**8**	**10**	**12**	**14**	**16**	**18**	**20**	**22**	**24**	**26**
Alpha	**4**	**12**	**20**	**30**	**37**	**39**	**40**	**40**	**40**	**40**	**40**	**40**	**40**	**40**
CnB	0	-0.0008	-0.0017	-0.0018	-0.0015	-0.0016	-0.0016	-0.0016	-0.0016	-0.0016	-0.0016	-0.0016	-0.0016	-0.0016
ClB	-0.0012	-0.0015	-0.0016	-0.00165	-0.0021	-0.002	-0.0021	-0.0021	-0.0021	-0.0021	-0.0021	-0.0021	-0.0021	-0.0021
Cnda	0.001	-0.0002	-0.00031	-0.00036	-0.0004	-0.00047	-0.0005	-0.0005	-0.00052	-0.00055	-0.00058	-0.0006	-0.0008	-0.00094
Clda	0.014	0.011	0.009	0.0122	0.015	0.0165	0.017	0.0173	0.0175	0.0176	0.0176	0.0177	0.02	0.021
IZZ/IXX	8.04	8.04	8.04	8.04	8.04	8.04	8.04	8.04	8.04	8.04	8.04	8.04	8.04	8.04
Calculations														
CnBdynamic	0.00067	0.00172	0.00280	0.00507	0.00896	0.00888	0.00963	0.00963	0.00963	0.00963	0.00963	0.00963	0.00963	0.00963
LCDP	0.00009	-0.00083	-0.00176	-0.00185	-0.00156	-0.00166	-0.00166	-0.00166	-0.00166	-0.00167	-0.00167	-0.00167	-0.00168	-0.00169

As we decelerate down to Mach 6, at *ALT*=150,000-ft at with dynamic pressure of 100-psf and attain 171-KEAS, as seen in FIGURE 20 and FIGURE 21, around the 1,600 second mark, we are now in a region where aerodynamic control "*should"* be reasonable. However, the shuttle aerodynamics continue to have poor *LCDP*; thus, absent RCS control power augmentation it has weak spin tendencies and roll-reversals. As the shuttle further decelerates and sinks deeper into the atmosphere to Mach 4, about the 1,700 second mark at an altitude of 90,000-ft and approximate dynamic pressure equaling 150-psf and attains ~245-KEAS, the shuttle is now in a region "C" where strong roll reversals result in control induced departure.

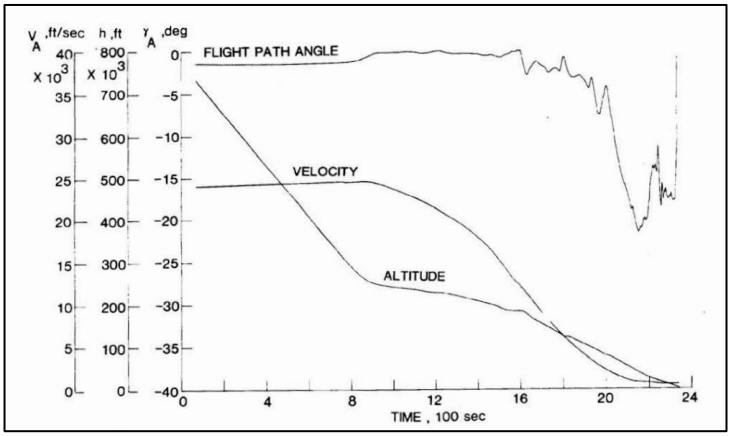

FIGURE 20. Flight Data Dynamic Pressure vs. Time [31].

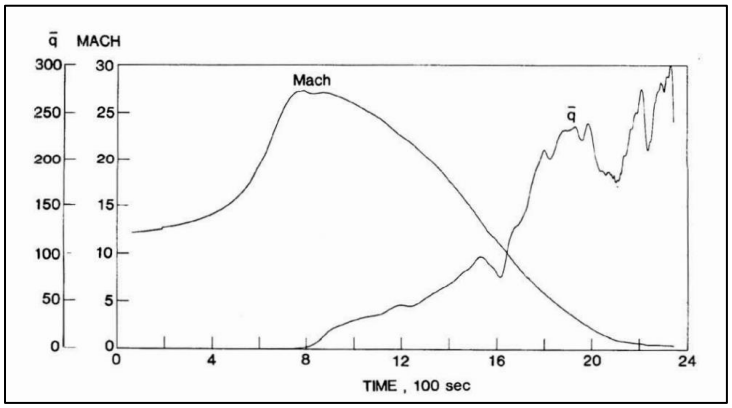

FIGURE 21. Flight Data Mach Number vs. Time [31].

At Mach 2, around the 1,900 seconds with a dynamic pressure of 170-psf, at an altitude of 65,000-ft and the nose is lowered to α = ~12°. We are now approaching the terminal area at ~225-KEAS. We are now in a region "F" with weak departure and spin resistance where controllability is heavily influenced by secondary factors.

On subsonic final gliding approach, where α = ~4° we remain firmly in region "F" with weak departure and spin resistance where controllability is heavily influenced by secondary factors. $Cn_{\beta DYN}$ is now quite small, once again highlighting the relatively weak static directional stability of the Orbiter (despite its visually imposing, large – but short coupled – vertical fin.)

Our interpretation of Bihrle Weissman criteria closely matches NASA flight operations results. In reality, the shuttle relied on its RCS thrusters in order to remain stable and controllable from initial reentry down to Mach 1.2 [34]. In another report, NASA specifically stated that "analysis indicated that the problem was caused by a sign change in the *LCDP* in the Mach 5 region. As a partial result of this problem, several changes were made to the (flight control system). The basic FCS design was changed from the aileron bank control to a system utilizing the yaw RCS jets to initiate bank maneuver and the ailerons to coordinate the maneuvers prior to activation of the rudder. After the rudder became active, a gradual FCS gain change produced the conventional aileron bank control with rudder coordination…. The orbiter FCS utilizes a side acceleration feedback to the rudder and yaw jets to provide stability augmentation." [41]

NASA further stated that, “Very little improvement is shown for the rudder augmentation. This is due to the small rudder effectiveness which results from the aeroelasticity effects and from application of aerodynamic variations. It is evident that the RCS provides a significant improvement…At the first bank maneuver which occurred very early in the entry, a large sideslip oscillation developed with β reaching a value of 3.5^{o}. Post flight analysis showed the primary culprit to be the rolling moment RCS jet interaction.” [34]

COMPUTATIONAL STUDY OF BASELINE SHUTTLE LATERAL-DIRECTIONAL CONTROLLABILITY

Subsonic/Supersonic Flight Regime of Baseline Model

The subsonic model was made in VORLAX. The geometry was taken from some NASA dimensions [39] shown below in FIGURE 7. The image was translated into an EXCEL Model to help in the creation of the panel geometry for VORLAX. The VORLAX panel model is shown in FIGURE 8. “VORLAX inputs a detailed geometry through a collection of panels to represent the aircraft airframe and control surfaces.... In addition to angle-of-attack, Mach Number, sideslip, and control surfaces deflections. The results are exported in an easily parsed text format.” [38]

The model was meant to capture key features such as leading-edge sweep along the wing and wing glove, wingspan, and the overall body dimensions. A feature that could not be captured in the model was the split flap in the vertical stabilizer. The combination of overlapping panels would not bode well for VORLAX.

Our VORLAX model had S_{ref} equal 2690 ft^2, $\bar{c}$ of 39.6 ft, and a wingspan of 78.1 feet. These all match the NASA dimensions [39]. The center of gravity for the model has a location of $\bar{x}$ of 71.40 ft and $\bar{z}$ of 12.5 ft [32][39].

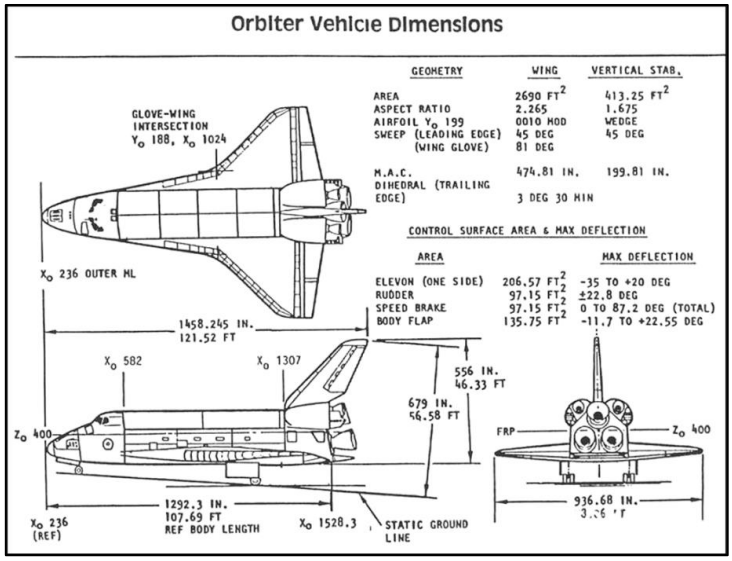

FIGURE 7. Orbiter Shuttle Dimensions [39].

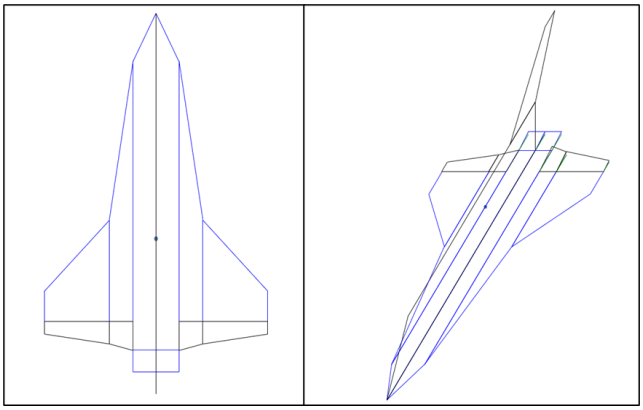
FIGURE 8. VORLAX Panels.

We further developed an aerodynamic database for the computational study through comparisons to subsonic data for corroborating wind tunnel and flight test data [42]. FIGURE 22 show the comparisons for basic aerodynamic parameters such as $C_{l_\beta}, C_{n_\beta}, C_{Y_\beta}, C_N, and\ C_m$. We see that there is a relatively close agreement between the VORLAX model and the subsonic wind tunnel and flight data. It is key to note that for the wind tunnel tests [42] the center of gravity was taken at 65% length which would be around 69.9 feet. This dimension was the forward limit of the vehicle, and the standard limit was considered to be 66.7% [32]. For the comparison to wind tunnel data [42] to validate our computational model, the CG of 65% was used as that is what the report indicated. Everywhere else in this report, the standard CG was used.

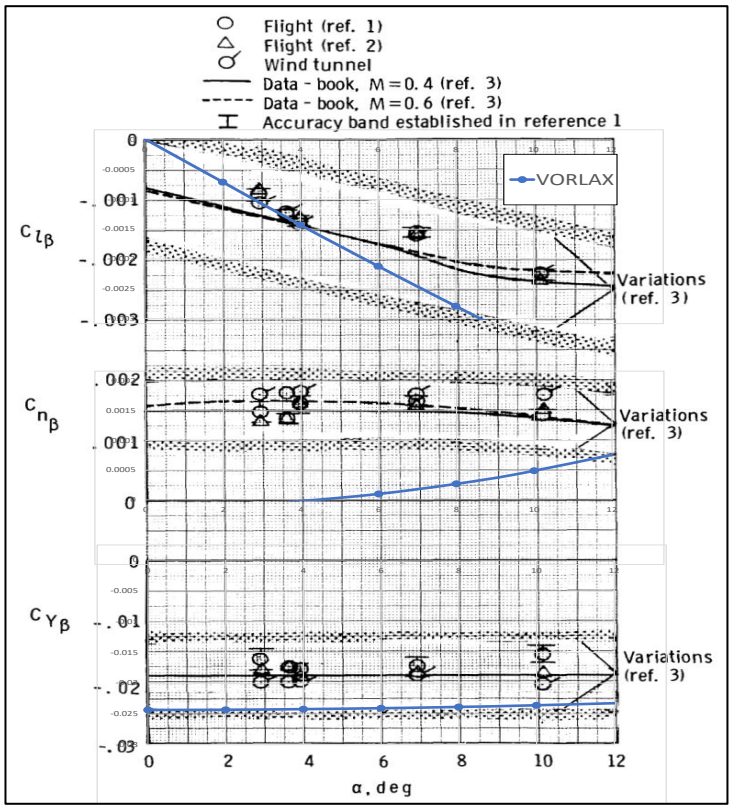

FIGURE 22. Subsonic Flight Data comparison to VORLAX $C_{l_\beta}, C_{n_\beta}, C_{Y_\beta}$ [42].

The magnitudes of the VORLAX results are within the variation with the exception of the yawing moment due to sideslip,Cn_β. This is due to the rudder effectiveness with the split flap. The split flap was deployed in flight test and the wind tunnel tests and cannot be modeled using the panel code. Notwithstanding, the panel method continues to match in accuracy to both the normal force C_N and pitching moment C_m. This is seen in the FIGURE 23.

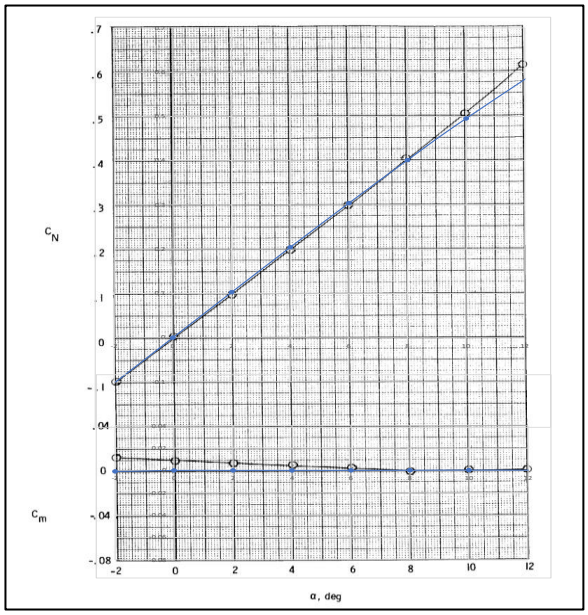

FIGURE 23. Subsonic Flight Data comparison to VORLAX C_N & C_m [42].

We see that for the shuttle at sideslip, the vehicle remains stable through all angles of attack. The positive nature of C_{n_β} helps to maintain yaw stability. The general negative behavior and decline in C_{l_β} represents an effective increase "Dihedral Effect" which leads to an overall stable rolling moment. The constant value and negative magnitude of the side force C_{Y_β} at sideslip further indicate the stability of the vehicle.

It is key to note that C_{n_β} is relatively close to zero. This indicates that the lateral-directional stability is fragile and could be influenced to be destabilized depending on flight trajectory and commands. In fact, the VORLAX model, which does not include the split flap, has a negative region which is unstable. The NASA report for the correlation of the wind tunnel data and flight test results from which the figures are pulled have only tests conducted split flap open configurations. This would seem as though the split flap feature may be necessary for stability and very fragile. This is evident in a NASA report [43], when they state, "Component buildup studies showed that the vertical tail contributed to the measured lateral and directional instabilities at the lower Reynolds numbers and angles of attack."

In the buildup study performed NASA [43] they concluded that the, "Component buildup studies showed that the vertical tail contributed to the measured lateral and directional instabilities at the lower Reynolds numbers and angles of attack…The most significant change in lateral stability incurred by removal of a configuration component[s]…The removal of the OMS pods in this case reduces the stability level…and the stability level is shown to increase slightly with the removal of the vertical tail" This illustrates the fragile nature of the lateral directional stability and its dependencies on the configuration.

Furthermore, we see that for the results of the computational study as they relate to the accuracy of the model, that the inability to model the split flap and the OMS pods would explain the differences in C_{l_β} but would otherwise be accurate. With the computational model showing to be relatively accurate, further comparison was made to verify the performance of the model and high Mach numbers.

Supersonic/Hypersonic Flight Regime of Baseline Model

The model was further run for Mach 0 to 30 and compared against known flight test data [44]. The results show the relative accuracy of VORLAX into high hypersonic. The results compare the sideslip derivatives specifically as they are key indicators to the directional-lateral stability of the vehicle. Furthermore, they help to illustrate the stability of the vehicle in a controls neutral state when perturbed.

We see that the for the side force coefficient at sideslip, C_{Y_β} in FIGURE 24 matches close to the overall trend and magnitudes of the flight test data. For the majority of the flight regime from Mach 2 to about Mach 18 the VORLAX results stay within the uncertainties bounds as well.

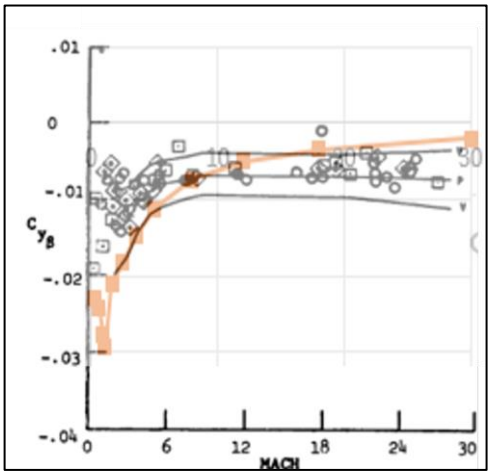

FIGURE 24. Hypersonic Comparison to VORLAX C_{Y_β}[44].

The pitching moment, C_{m_α}, matches relatively well as seen in FIGURE 25. It is observed that the VORLAX results match the initial and higher Mach values of the flight test data but deviate between Mach 1 till about Mach 2.5.

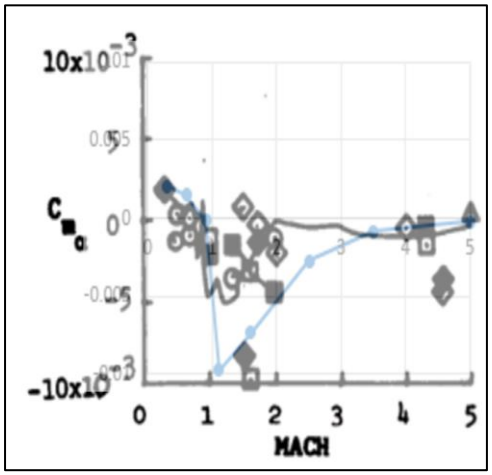

FIGURE 25. Hypersonic Comparison to VORLAX C_{m_α}[44].

For C_{n_β} and C_{l_β}, seen in FIGURE 26 and FIGURE 27 respectively, the VORLAX results vary from the flight test results. For C_{n_β} in FIGURE 26, although the VORLAX results do not match in magnitudes to the flight test results, they do match in trend. They both rise and sharply decline below MACH 6 and then plateau till the top of the flight regime. This would validate the VORLAX ability to predict trends while the results may vary in scale. This however not true for C_{l_β} in FIGURE 27. We see that the trend nor the magnitudes of the VORLAX results do not match the flight test results. This inconsistency is okay as it is explainable with the subsonic VORLAX model and the results of the subsonic wind tunnel test.

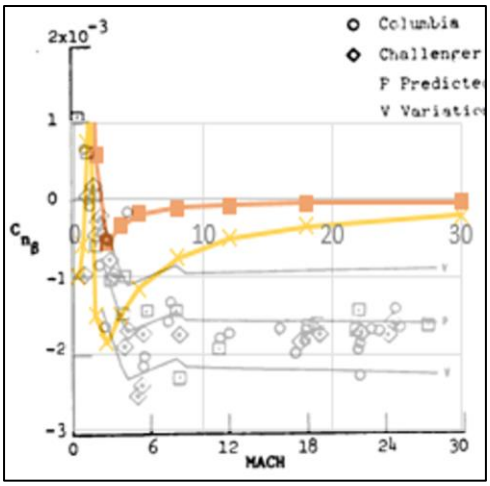

FIGURE 26. Hypersonic Comparison to VORLAX C_{n_β}[44].

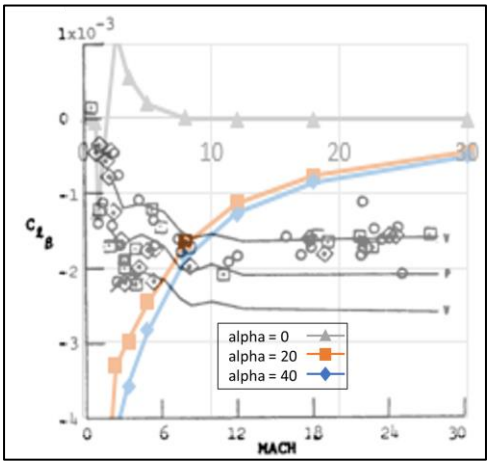

FIGURE 27. Hypersonic Comparison to VORLAX C_{l_β}[44].

It was in the component buildup study mentioned earlier that it was found that the stability depended more on the OMS pods than the vertical tail. Therefore, with the VORLAX results being constrained to only utilizing the vertical tail, the inaccuracy could be written off and can be used to further illustrate the need for other configurations to augment the stability of the vehicle.[43]

The computational shuttle baseline model in VORLAX proves to be relatively accurate from low speed to high speed through all angles of attack. It even proves to be relatively accurate for the lateral-directional results at hypersonic speeds. It further presents the understanding of the Shuttles basic stability as passes through its flight regime. We see that the Orbiter has relatively fragile stability; it is highly dependent on the RCS for augmented stability. We note that the lateral-directional derivatives are highly dependent on configuration.

Hypersonic flight involves real gas and viscous effects both of which are not within the capability of the inviscid methods of VORLAX. The accuracy of the results are predicated upon the validation to the flight test and wind tunnel results. We showed that the VORLAX results are accurate in trend and magnitude to the flight data. In addition to the relatively small values of the yaw, pitch, and roll coefficients that exist in the hypersonic regime, the VORLAX results do not misrepresent those values either. Therefore, we constrained our results to Mach 6, to ensure that the results stay true to the flight test results and ensure that, notwithstanding VORLAX's lack of capability to model real gas and viscous forces, the results can still be valid in this specific case.

Computational Baseline Shuttle Lateral-Directional Controllability

Lateral-directional controllability can be evaluated through comparison of $C_L, dC_n/d\beta, dC_l/d\beta$ versus alpha and Mach number. From the above section it is noted that the rolling moment (C_l) and yawing moment (C_n) are both slightly inaccurate. With the rolling moment being off in both trend and magnitude while the yawing moment was off by magnitudes while maintaining accurate trends. Notwithstanding, the FIGURE 28 through FIGURE 31 (below) show the baseline shuttle lateral-directional controllability.

As mentioned above, the center of gravity for the wind tunnel test [42] was taken to be 69.9 feet, the forward limit on the vehicle. For the paper 71.40 was used due to it being the standard location [32]. Figures 28 through 32, panels “a” and “b” respectively represent the difference between the two CG locations. Thes shifting of the CG location effects the pitching and yawing moments.

The coefficient of lift C_l in FIGURE 28a and 28b trends in an expected fashion. It increases as Mach increases. However, at Mach 2, it drops to become the lowest in the family.

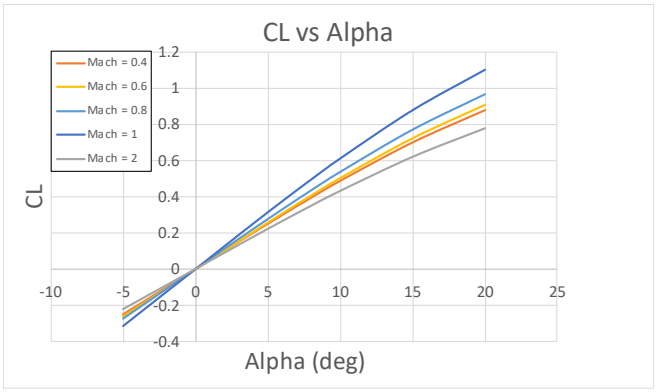

FIGURE 28a. Baseline Shuttle C_L vs α CG-69.9 feet.

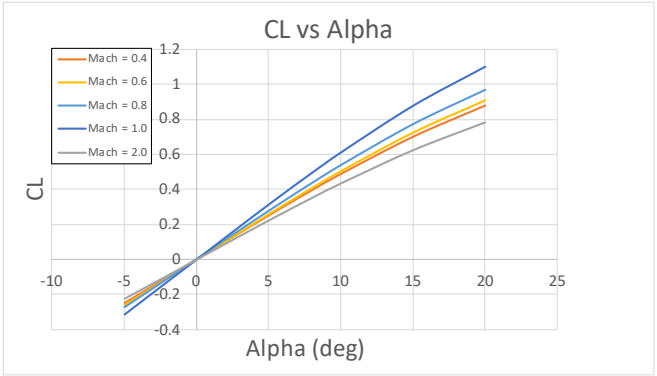

FIGURE 28b. Baseline Shuttle C_L vs α CG-71.40 feet.

FIGURE 29a shows C_l versus C_m. This plot illustrates the increasing stability of the vehicle as Mach increases. We see that for Mach 0.4, the results trend towards the positive C_m values as C_L increases. At higher Mach numbers, the C_m values become more negative as C_L increases. This would represent a downward pitching moment as lift increases. However, for FIGURE 29b this is not true. Nose down only above Mach 1 and Mach 2. At the slower Mach numbers, the more aft CG dominates the pitching stability and drives a nose-up motion.

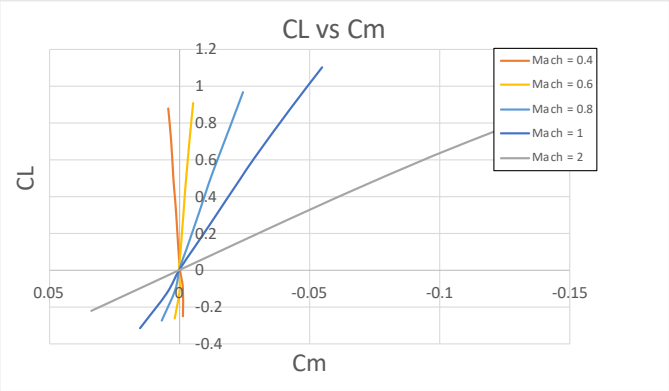

FIGURE 29a. Baseline Shuttle C_L vs C_m CG-69.9 feet.

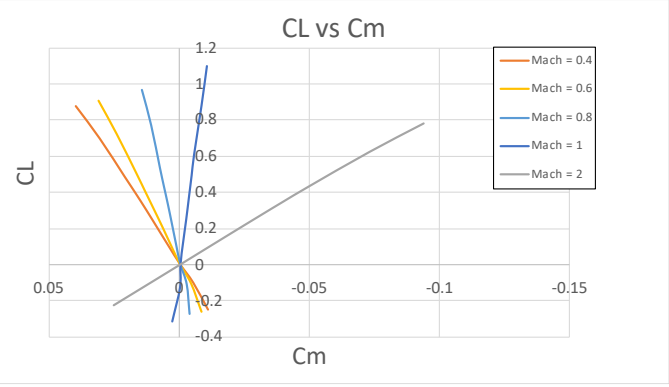

FIGURE 29b. Baseline Shuttle C_L vs C_m CG-71.40 feet.

The yawing moment shows stable as Mach increase through all the angles of attack. FIGURE 30a and 30b shows that as Mach increases, the values of the results increase. The shifting in CG does indeed shift the results to be more unstable. This is illustrated in the general shift downward of all the results to be more negative.

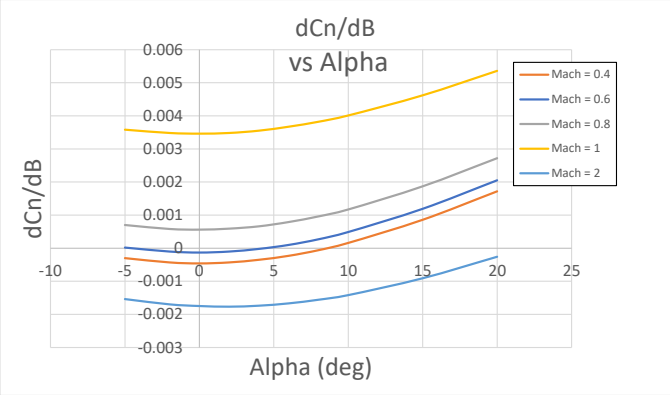

FIGURE 30a. Baseline Shuttle $dC_n/d\beta \; vs \; \alpha$ CG-69.9 feet.

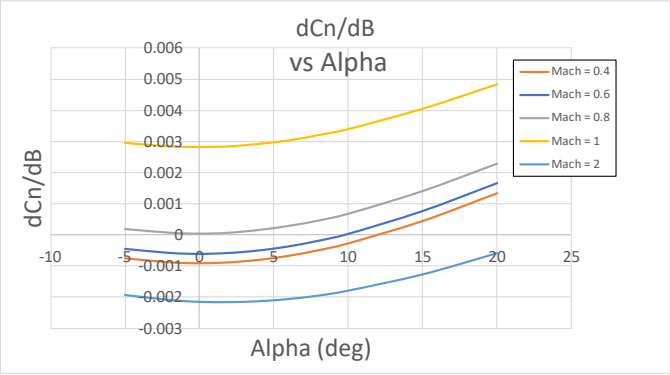

FIGURE 30b. Baseline Shuttle $dC_n/d\beta \; vs \; \alpha$ CG-71.40 feet.

For FIGURE 31a and 31b (below), the rolling moment becomes more negative, thus increasing in "Dihedral Effect" through the supersonic flight regime. This is seen in the overall decreasing values of $dC_L/d\beta$ for Mach 0.4, 0.6 and 0.8, with a large jump in positivity to Mach 1 and even larger jump to Mach 2 After supersonic flight the "Dihedral Effect" begins to reduce in strength.

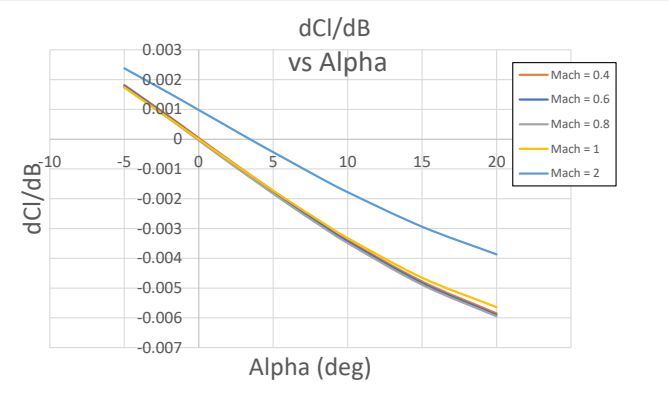

FIGURE 31a. Baseline Shuttle $dC_l/d\beta \; vs \; \alpha$ CG-69.9 feet.

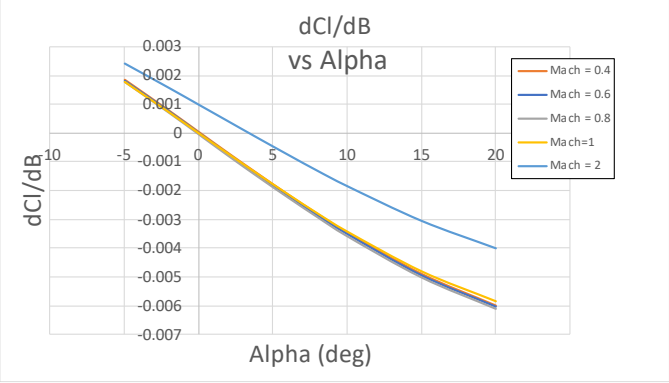

FIGURE 31b. Baseline Shuttle $dC_l/d\beta \; vs \; \alpha$ CG-71.40 feet.

Overall, the shuttle is stable in subsonic to supersonic flight albeit very fragile. The fragile nature of the stability of the vehicle is seen throughout as for every graph presented, there are regimes in which the vehicle has an unstable mode. At supersonic speed, the rolling moment and yawing moment go positive which destabilize the vehicle. At low speeds, the rolling and yawing become manageable while the pitching moment becomes negative and a problem.

OBSERVATION THAT LATERAL-DIRECTIONAL STATIC STABILITY DEPENDS ON LONGITUDINAL TRIM

During our "calibration" process, reverse engineering the Shuttle Orbiter aerodynamics with panel method codes, we observed a fascinating phenomenon: that the static lateral-directional stability of the Orbiter depended upon Longitudinal Trim.

Classical aircraft stability and control analysis considers both longitudinal and lateral-directional stability to be decoupled from trim. Yechout [25] represents the dominant paradigm; the equations of motion are expressed in terms of three forces (lift, drag and side force) and three moments (pitching, yawing and rolling) about one of the customary axis systems (either body aligned, earth aligned or in "stability" axis). The forces and moments, respectively, derive from a first order Taylor series with the following characteristic form; for pitch:

$$Cm = Cm_0 + dCm/d\alpha\ \alpha + dCm/delev\ \delta elev + \ldots.$$

And more importantly, for yaw:

$$Cn = Cn_0 + dCn/d\beta\ \beta + dCn/daileron\ \delta aileron + dCn/drudder\ \delta rudder$$

And roll:

$$Cl = Cl_0 + dCl/d\beta\ \beta + dCl/daileron\ \delta aileron + dCl/drudder\ \delta rudder$$

This nomenclature and approach to the flight dynamics is pervaisive throughout the aircraft industry. We have seen above, in Figures 22 through 23, how NASA reduced both wind tunnel and flight test data to fit this paradigm.

What we have come to realize is that the "stick fixed" derivatives of slender, "delta wing" configurations such as the Shuttle Orbiter are dependent upon nuances of collective and anti-symmetric deflections of the elevons.

Consider that slender configurations develop considerable "dihedral effect," rolling moments due to sideslip, as a byproduct of their swept wings. Returning to FIGURE 32, we see that the sweep effect on dihedral effect is strongly dependent on angle of attack. Consider that the aircraft has wings swept at angle Λ ; and will fly at sideslip β. Sweep dependent rolling moments due to sideslip at angle-of-attack form because the yawed geometry is assymmetric from the perspective of the oncoming wind. Rolling Moment Due to Sideslip is due to both the asymmetric span-wise distribution of lift and vertical distribution of side-force elements. The first term arises because one wing displays less sweep with the opposite wing displays more sweep. With asymmetric flow, one wing will develops more lift than the other (recall that $dCL/d\alpha \sim \cos(\Lambda +/- \beta)$) thus inducing a rolling moment about the center-of-gravity. Similarly, forces produced by the vertical tail will induce roll. Since the vertical tail forces are proportional to sideslip angle, b, they generates moments depending upon vertical displacement of lift centroid above c.g. A dorsal vertical will produce a negative rolling moment from positive sideslip ($dCl/d\beta<0$) whereae a vental vertical will produce a positive rolling moment from positive sideslip ($dCl/d\beta>0$); refer to FIGURE 32 below.

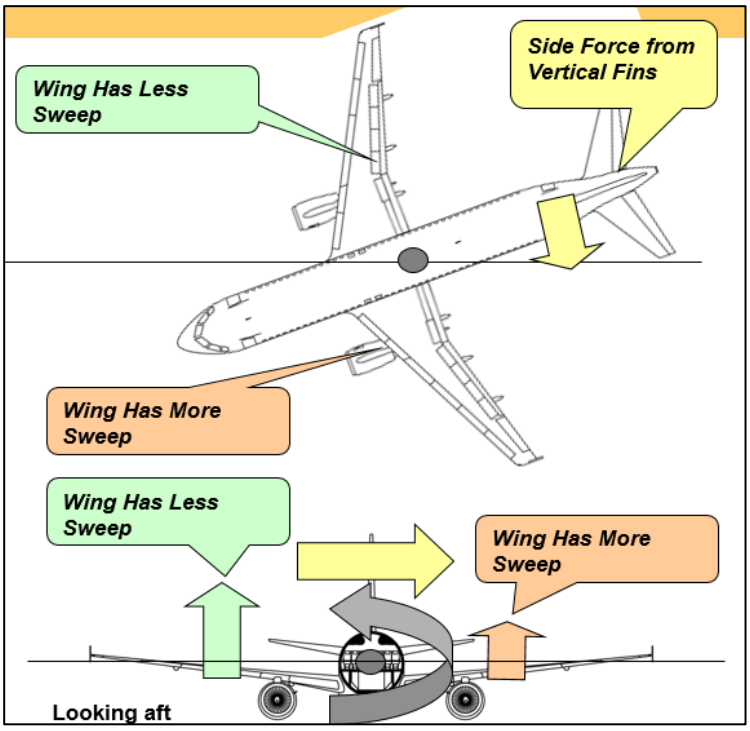

FIGURE 32. How Wing Sweep and Vertical Tail Disposition Impact $dC_l/d\beta$.

Turning to our VORLAX model of the Space Shuttle Orbiter, we can visualize the asymmetry in lift. Consider FIGURE 33 for a surface color map of the net pressure differential across each panel for the Orbiter at Mach 0.3, α =10° and β =0°. For FIGURE 33a, we see the net lift distribution over the vehicle with controls neutral; the strong leading edge suction on the main wing is clearly evident as are the relatively unloaded elevon panels. In FIGURE 33b, we see the results with the elevons deflected trailing edge down 17°; in the process of commanding the nose down moment they also induce noticably stronger lift over the entire wing. Similarly, in FIGURE 33c, with the elevons deflected trailing edge up 17°; we see how they reduce lift over the entire wing. Thus, it should be of no surprise, that the sideslip behavior of the Orbiter depends upon collective elevon deflection.

A) Elevons Neutral B) Nose Down C) Nose Up

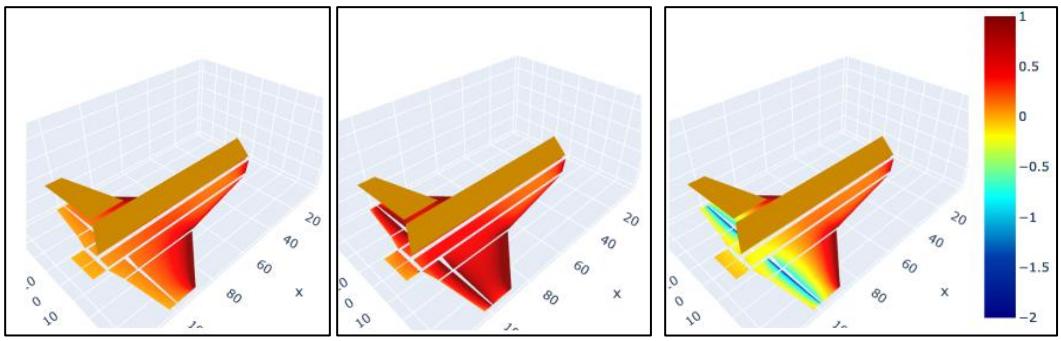

FIGURE 33. Shuttle Orbiter – net ΔCp *MACH 0.3 α = 10, β=10, vs β =10 with elevators neutral, nose down, nose up.*

FIGURE 34 (below) demonstrates how strongly collective elevon impacts the lateral-directional stability of the Orbiter. At subsonic speeds, as modelled here, 17^{o} of collective elevon can change the overall dihedral effect ($dCl/d\beta$) by +/- 25% at α=10^{o}; see FIGURE 34a. The impact on weathercock, directional stability ($dCn/d\beta$) is +/- 50% at α =10^{o}; see FIGURE 34b. Note that since the Orbiter is essentially neutrally stable in yaw, small changes in that directional stability derivative makes for large percentage change. This phenomenon, while not discussed in some classical texts, is hardly unique to the Shuttle Orbiter – it should plague all slender vehicles's with weak static directional stability.

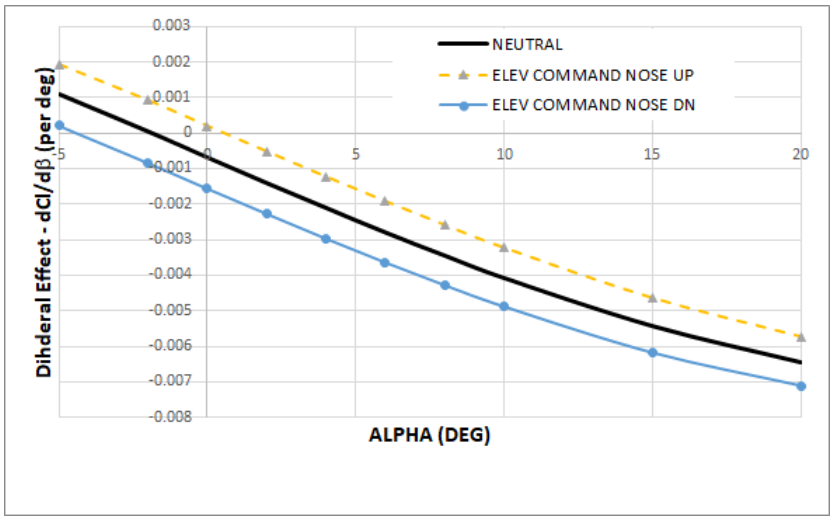

FIGURE 34a. VORLAX Subsonic Estimates of Static Lateral-Directional Stability *As* dCl /d*β*, *a function of collective elevon deflections – elevators neutral, nose down, & nose up.*

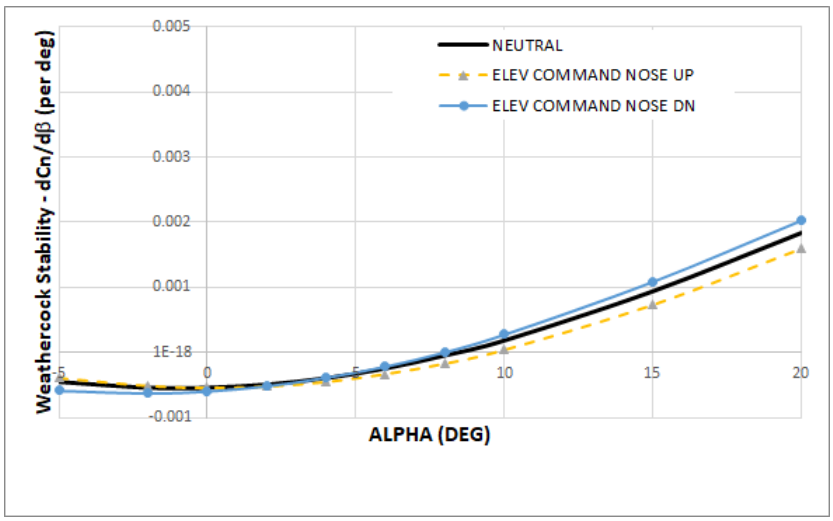

FIGURE 34b. VORLAX Subsonic Estimates of Static Lateral-Directional Stability *As* dCn /d*β*, *a function of collective elevon deflections – elevators neutral, nose down, & nose up.*

UNDERSTANDING HOW LONGITUDINAL TRIM STRATEGY IMPACTS THE LATERAL-DIRECTIONAL BIHRLE WEISSMAN CRITERIA

Longitudinal Trim

The shuttle uses a combination of body flap and elevon commands to longitudinally trim the vehicle. The trim of the shuttle had impact on the lateral-directional stability. As stated above the shuttle had very weak stability and was neutrally stable in yaw. It relied heavily on the RCS to augment the stability through hypersonic flight. However, the stability of vehicle seemed more dependent on the configuration versus the flight regime.

The shuttle with the body flap has basically four combinations of longitudinal trim settings. Those being the body flap trimmed up or trimmed down with the elevons likewise trimmed up or down. With both features impacting the longitudinal trim, it was important to understand how the control surfaces would interact with the other.

A study was conducted sweeping through the elevator trim settings from -10 degrees to 10 degrees while varying the body flap through the same sweep angles. Negative trim angles represent control surfaces downward and vice versa for positive angles. See FIGURE 35 below for definition. Two body flap settings are shown in FIGURE 36 and FIGURE 32.

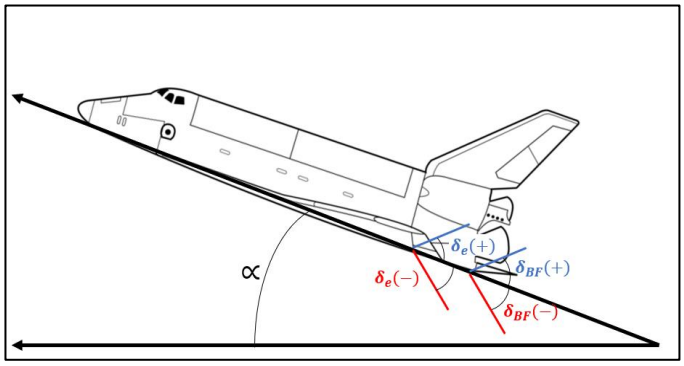

FIGURE 35. Elevator Direction Definition [45].

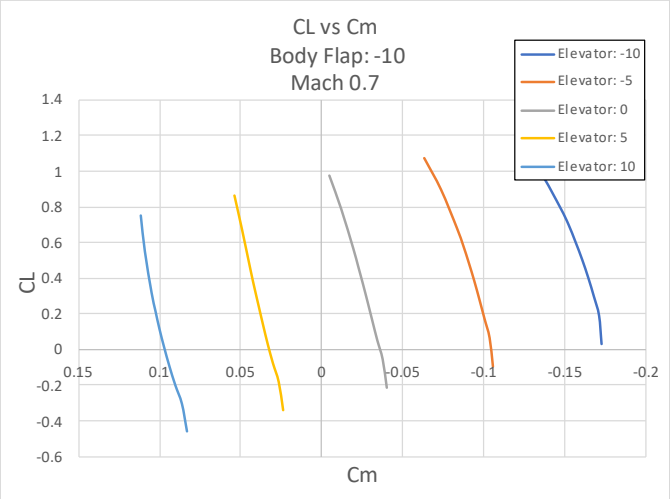

FIGURE 36. C_L vs C_m Various Elevator Mach 0.7 Settings BF: -10.

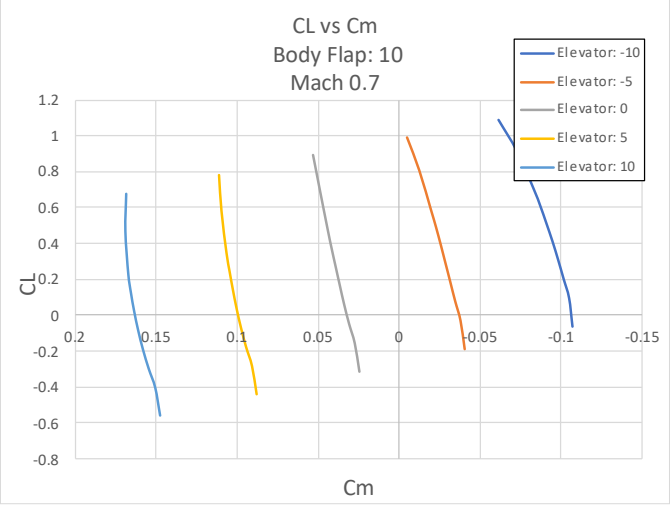

FIGURE 37. C_L vs C_m Various Elevator Mach 0.7 Settings BF: 10.

A more negative pitching moment (C_m) results in a stabilizing nose movement of the aircraft. Increases in the coefficient of lift (C_L) could be attributed to increases in angle of attack (α) or increases in Mach number. Thus, lift coefficient versus pitching moment graph is a good indicator of longitudinal stability as it can represent perturbations in flight that would cause nose upward movements and the ability the aircraft has to correct nose down. For FIGURE 36 and FIGURE 37 the Mach number was held constant, and the angle of attack was varied form -5 degrees to 20 degrees.

For FIGURE 36 with body flap of -10 degrees the untrimmed vehicle is stable. This is seen in the gray line for elevator setting of zero degrees is negative as lift coefficient increases. This is contrasted by the body flap setting of 10 degrees. The gray line for elevator trim of zero is resulting in positive pitching moments for increasing lift coefficients. This shows that for control surfaces neutral, the body flap is sufficient to command either nose up or nose down. In fact, it is strong enough in a trimmed upward position to overcome the elevator trim strength. This is seen in FIGURE 37 where the elevator of -5 degrees is barely negative as lift coefficient is peaks. The peak lift coefficient is achieved at alpha of 20 degrees.

Therefore, at positive body flap and high angles of attack, stability will be weak and will require more negative trim to command nose down. Luckily, the trajectory of the shuttle at high speed and high angles of attack was intending to maintain a nose up position to aerobrake upon reentry. Hence the use of RCS thrusters at hypersonic speeds in the upper atmosphere and decent.

At lower Mach numbers in the flight trajectory when NASA wanted to begin to command nose down and pilot the vehicle into final, around Mach 2-ish, we see that shuttle would have a healthy, stable, pitch downward motion. TABLE 1 shows that Mach 2, with elevon of 5 degrees, body flap of -4 degrees, and alpha of 12 degrees corresponds to the run of body flap of -5, alpha of 10 degrees, and elevator of 5 degrees at Mach 2. This confirms the accuracy of VORLAX and illustrates that the vehicle could use combinations of body flap elevator to trim the vehicle.

The pitching moment of zero or C_{m_0} represents the Orbiter's longitudinal pitch stability as it is the point where the vehicle will nose or down. For supersonic flight, we see in FIGURE 38 and FIGURE 39 that the pitching moment trends the same for the body flap settings yet only shifts vertically in relation to lift coefficient (C_L). This is noticed most prominently in the gray line of zero elevator. It goes from a negative C_L at $C_{m_0}(C_m = 0)$ for negative body flap to a positive C_L at zero C_m for positive body flap. The converse is true for subsonic trim condition. For a negative body flap setting at zero elevator in FIGURE 38 a positive C_L at $C_{m_0}(C_m = 0)$ occurs while negative C_L at zero C_m for positive body flap. See FIGURE 40 for relationship.

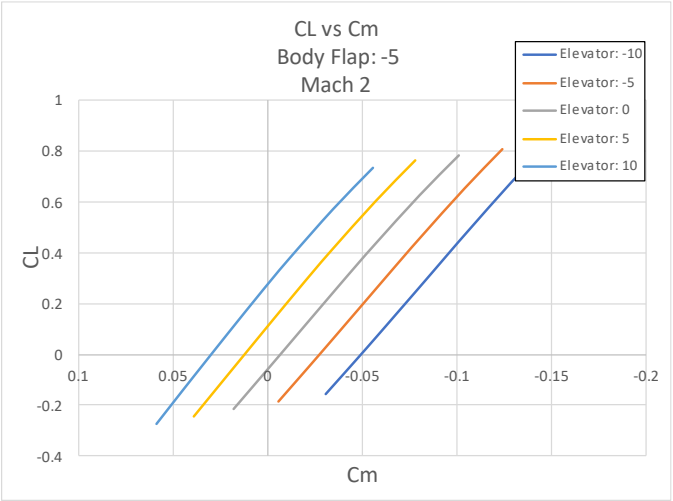

FIGURE 38. C_L *vs* C_m Various Elevator Mach 2 & BF: -5.

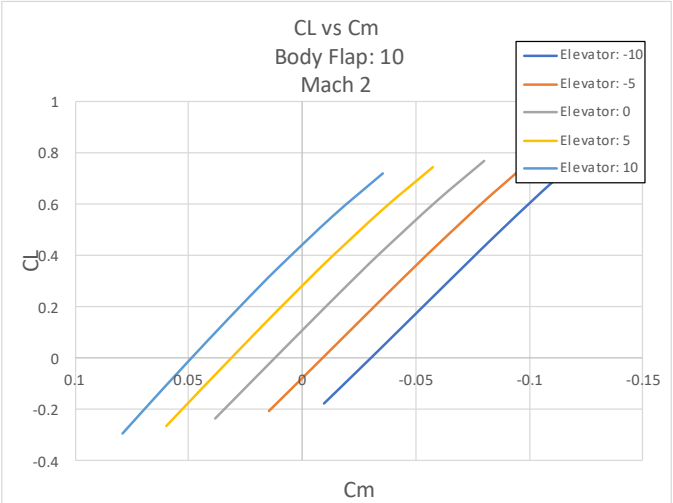

FIGURE 39. C_L *vs* C_m Various Elevator Mach 2 & BF: 10.

BodyFlap \ Mach	Subsonic	Supersonic
Positive	(-) CL @ Cm0	(+) CL @Cm0
Negative	(+) CL @Cm0	(-) CL @ Cm0

FIGURE 40. C_{M_0} Matrix.

We note that for both supersonic and subsonic cases. Whereas the body flap can potentially command nose up and nose down, the stability of the vehicle was dominated heavily by the elevator trim. This interaction between the body flap and elevator was further investigated when maintaining for setting a specific elevator and setting and varying the body flap from positive to negative. FIGURE 41 through FIGURE 44 show how the vehicle responds for holding the elevator trim constant at subsonic and supersonic speeds and varying the elevator.

We see that by varying the body flap had some impact at singular elevator trim points. It can see from the blue arrows in the figures that variance in body flap seems to degrade the pitch down performance of the vehicle. This is true for all settings. Those being trimmed up and down for subsonic and supersonic.

Where negative body flap and negative elevator should command nose down at subsonic cases, even at positive body flap, the vehicle can still command nose down. This is seen throughout the graphs below, FIGURE 41 through FIGURE 44, and therefore it can be concluded that the elevators dominate the trim ability of the vehicle.

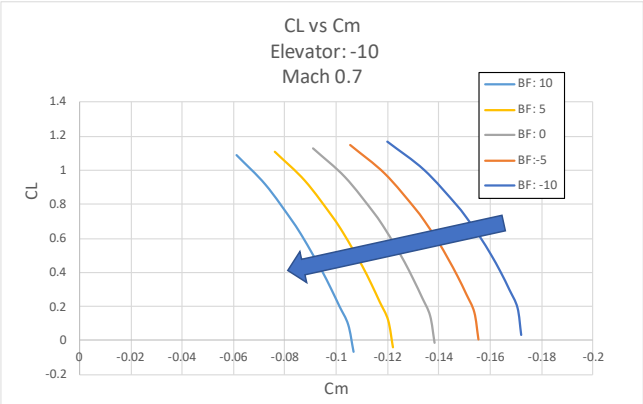

FIGURE 41. C_L vs C_m Mach 0.7 Elevator: -10.

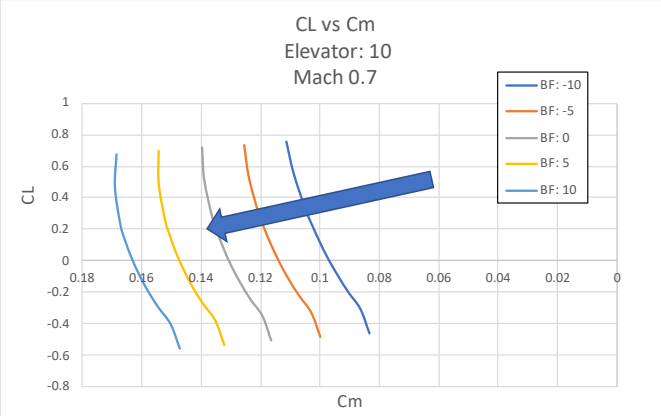

FIGURE 42. C_L vs C_m Mach 0.7 Elevator: 10.

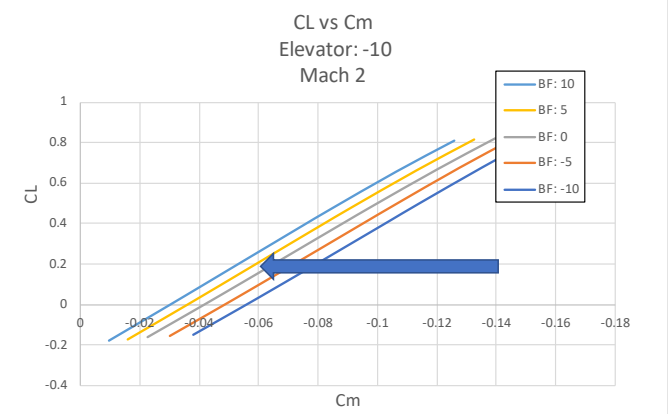

FIGURE 43. C_L vs C_m Mach 2 Elevator: -10.

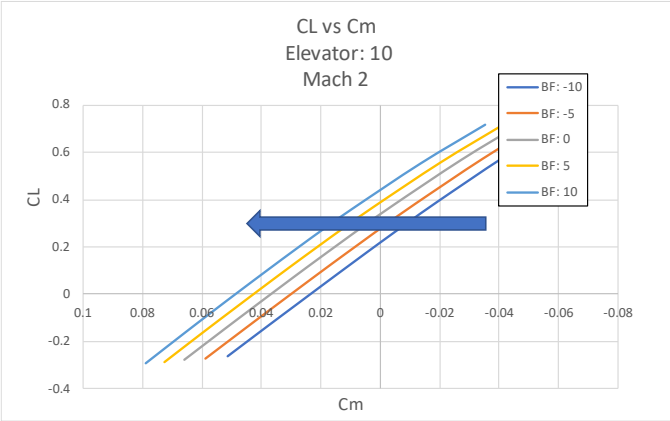

FIGURE 44. $C_L \; vs \; C_m$ Mach 2 Elevator: 10.

Lateral-Directional Trim Effects Only

We examined the lateral-directional capabilities of the Orbiter using the same process. That being the sweeping the body flap through the previously mentioned angles of -10, -5, 0, 5, and 10 degrees while also sweeping through those very same angles for the elevator trim. For yaw and roll however they were analyzed at a sideslip beta. Those results are shown in FIGURE 45 through FIGURE 51.

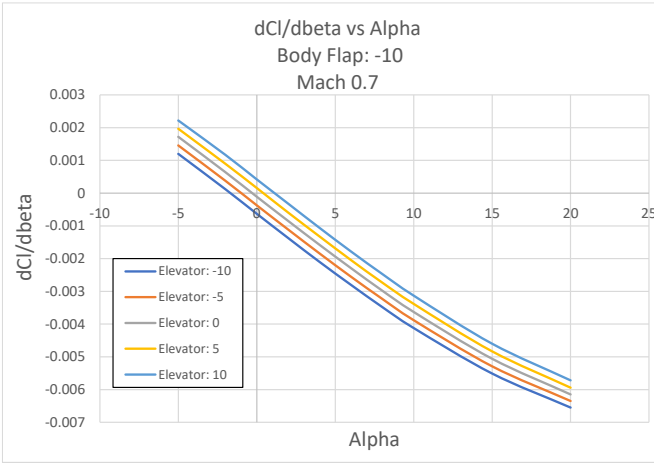

FIGURE 45. $dC_l/d\beta \; vs \; \alpha$ BF: -10 Mach 0.7.

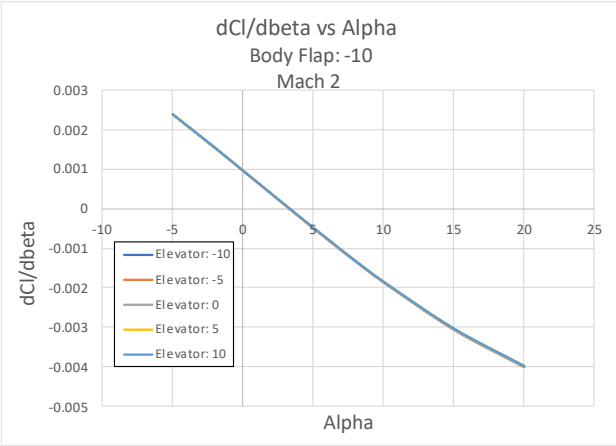

FIGURE 46. $dC_l/d\beta \; vs \; \alpha$ BF: -10 Mach 2.

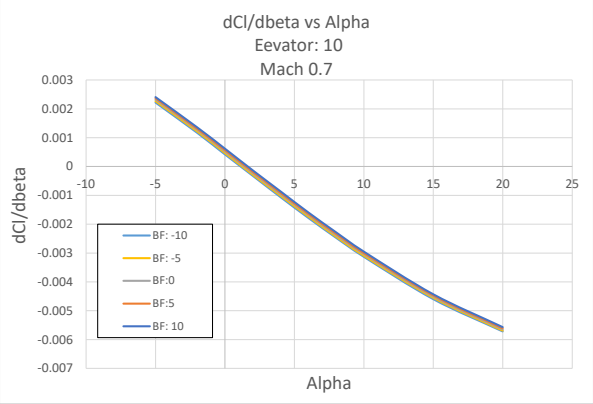

FIGURE 47. $C_l/d\beta \; vs \; \alpha$ Elevator: 10 Mach 0.7.

We see that for rolling moment (C_l) that body flap seems to have no effect in either the subsonic, FIGURE 45, or supersonic flight regime, FIGURE 46. For the supersonic regime, FIGURE 46, rolling moment is independent of elevator and body flap. However, the elevator trim setting does seem to affect the rolling moment stability at subsonic speeds, FIGURE 45. It shifts the (C_{l_0}). The rolling moment has an ever increasing "dihedral effect" which is good for the vehicle. However, at supersonic speeds, FIGURE 46, there are portions, (below angle of attack $(\alpha) = 5^o$), in which it is unstable.

Similarly, the yawing moment (C_n) showed no dependence on body flap setting. This is seen in FIGURE 48 and FIGURE 50. The body flap settings all overlay. Mach number does indeed affect the stability. In FIGURE 48 its stable and increasing in stability while in FIGURE 50 it is unstable but increasing. This is contrasted by FIGURE 49 and FIGURE 51 where at single body flap setting, there is a spread of curves depending on elevator trim.

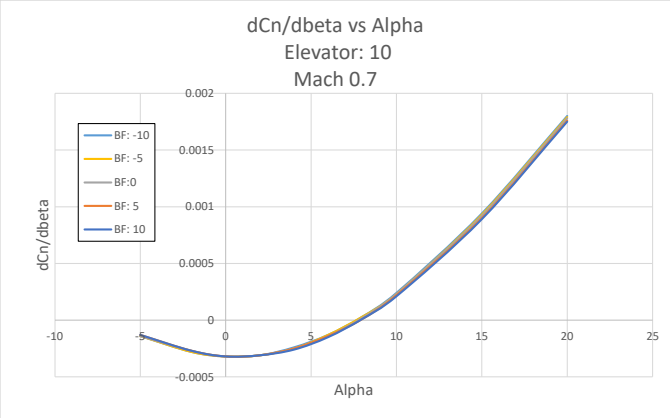

FIGURE 48. $dC_n/d\beta\ vs\ \alpha$ Elevator 10 Mach 0.7.

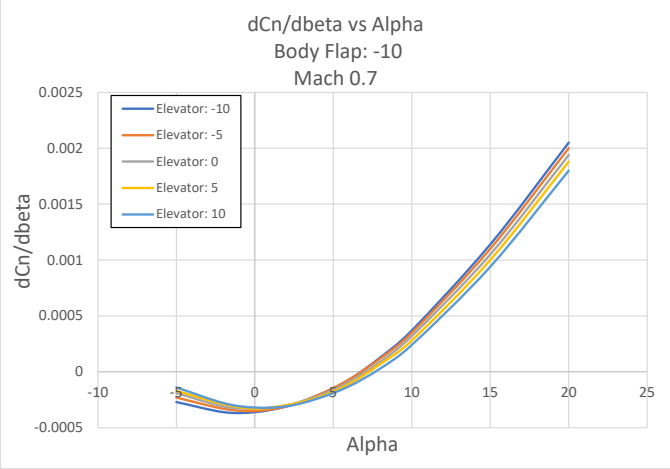

FIGURE 49. $dC_n/d\beta\ vs\ \alpha$ Body Flap -10 Mach 0.7.

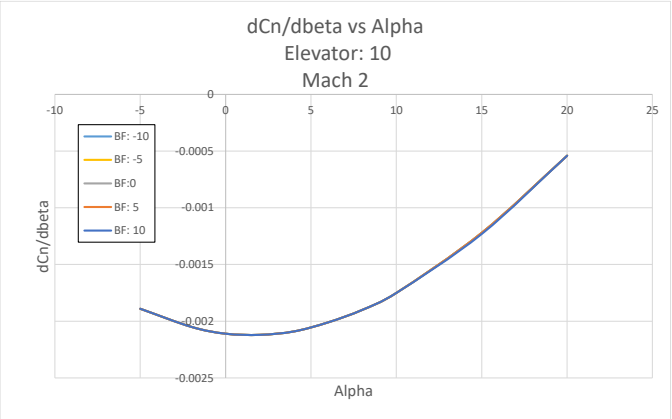

FIGURE 50. $dC_n/d\beta\ vs\ \alpha$ Elevator 10 Mach 2.

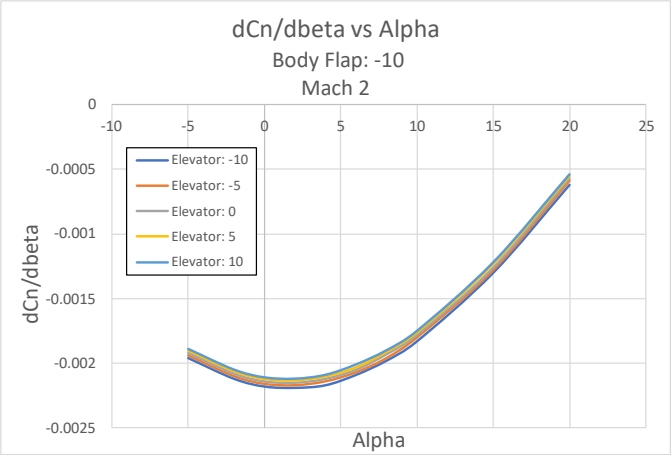

FIGURE 51. $dC_n/d\beta\ vs\ \alpha$ Body Flap -10 Mach 2.

Overall, we see that elevator does indeed affect the lateral-directional stability of the vehicle. Furthermore, speed as well greatly affects the stability of the vehicle. Where body flap does not impact as much the lateral-directional values of roll and yaw as much as it does pitch, elevator trim does move depending on trim and speed.

Lateral-Directional Differential Effects

We also analyzed the impact on differential aileron on lateral-directional stability. Our study looked at the same elevator trim control points and body flap points as the above-mentioned sections. Those being the -10, -5, 0, 5, and 10°. The elevator would trim to a given control point and then move +/- 1° from that point. This would be the aileron movement. An elevator trim of 10 degrees with aileron differential of +/- 1° would result in the right elevon total differential being 11 degrees and the left elevon being 9°. Pitch for these studies remain unchanged from the previous results. FIGURE 52 through FIGURE 54 are the results on roll and yaw.

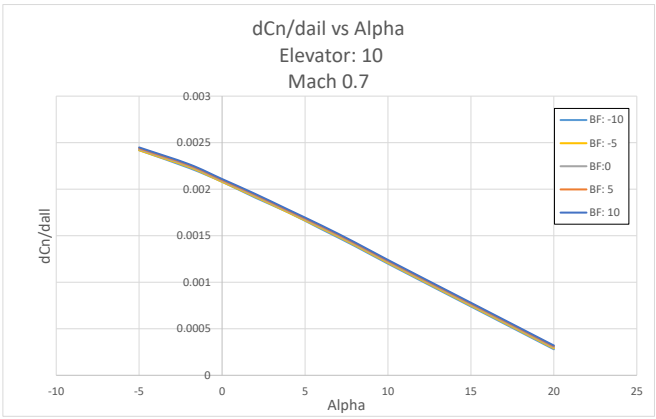

FIGURE 52. $dC_n/dail\ vs\ \alpha$ Elevator 10 Mach 0.7.

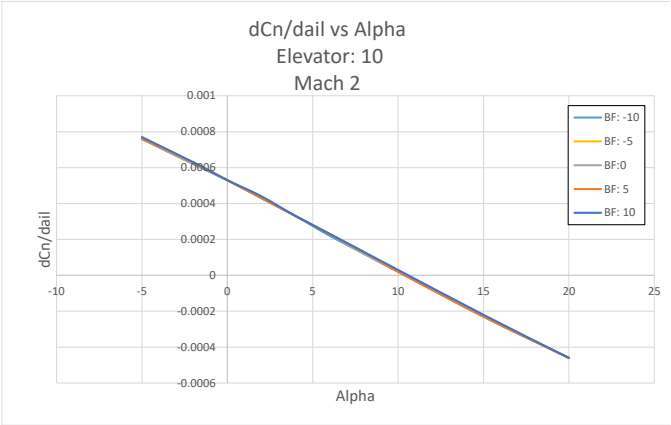

FIGURE 53. $dC_n/dail\ vs\ \alpha$ Elevator 10 Mach 2.

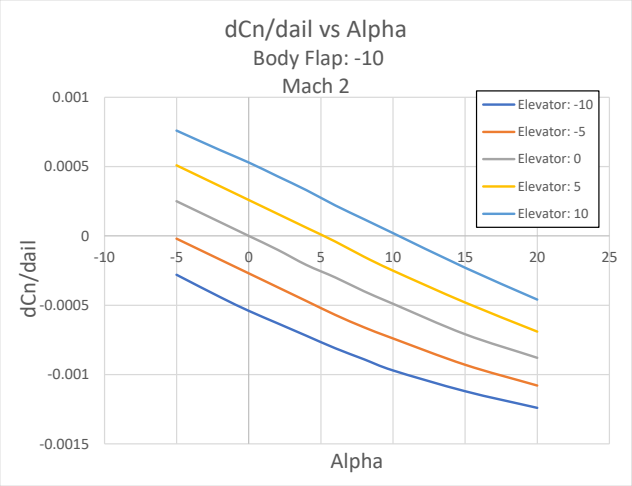

FIGURE 54. $dC_n/dail\ vs\ \alpha$ BF: -10 Mach 2.

We observe that for the yawing moment at elevon differential, body flap has no impact. This is seen in FIGURE 52 and FIGURE 53 where the lines are all coincident. It is however dependent on elevator trim and Mach. Comparing FIGURE 52 and FIGURE 53, the Mach 2 case is much weaker in yaw than the Mach 0.7 case. The Mach 0.7 case has stability throughout all the angles of attack, alpha, as the resultant yawing coefficient (C_n) stays positive. This is not the case for Mach 2 as it becomes negative at higher angles of attack. (FIGURE 53) In addition to the Mach dependency, there is an impact of elevator trim as well. This is illustrated in FIGURE 54 as there is noticeable spacing between all the elevator settings. It appears that at high positive elevator trim, there is some stability in yaw, but still drops off at high angles of attack. This dependency on Mach number and high angles of attack becomes crucial for the nature of the vehicle's stability. As it requires high angles of attack at hypersonic speeds for aerobraking on reentry, this becomes detrimental to the Orbiter's performance and requires some stability augmentation. Rolling moment results are shown in FIGURE 55 through FIGURE 57.

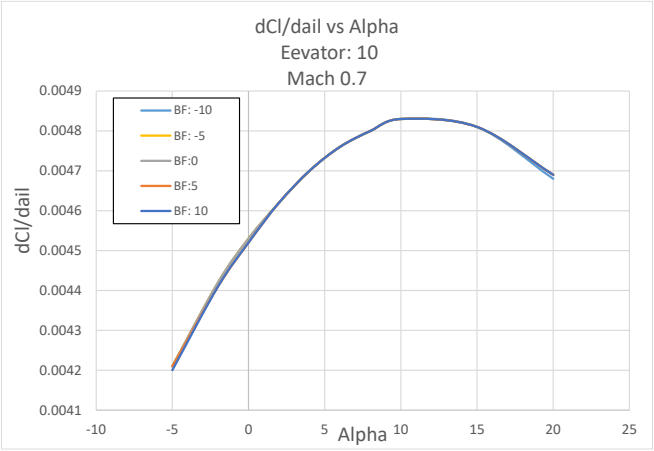

FIGURE 55. $dC_l/dail\ vs\ \alpha$ Elevator 10 Mach 0.7.

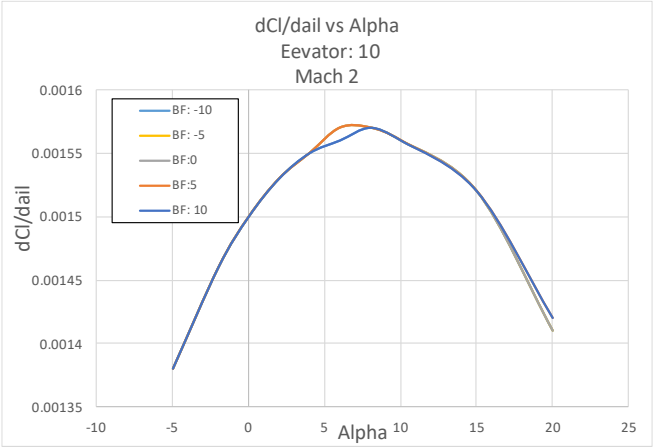

FIGURE 56. $dC_l/dail\ vs\ \alpha$ Elevator 10 Mach 2.

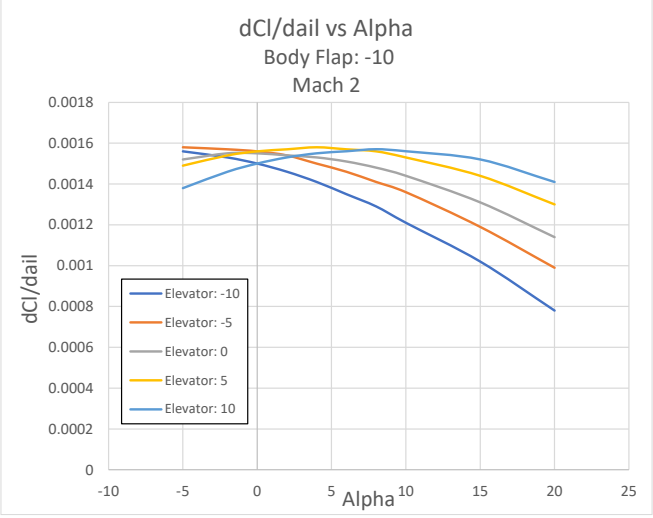

FIGURE 57. $dC_l/dail\ vs\ \alpha$ BF: -10 Mach 2.

Similar to yawing moment, rolling moment (C_l) responds in a similar fashion. That being that the response is independent of body flap and dependent on Mach number and elevator trim. However, unlike the yawing moment results, the rolling moment is unstable. This is seen in the overall positivity of the results where they should be more negative. This could be due to the inability of modeling the OMS pods as mentioned above. Notwithstanding the vehicle is still unstable. These effects were further analyzed using a Bihrle-Weissman chart.

The model of the shuttle would run an elevator neutral case at a sideslip of β of 1^o with elevator deflection varying between α of $0^o, 1^o, 3^o,$ and 5^o. The aileron deflection was taken from α of -4^o to 15^0 in increments of 2^o, except for the last point. The varying of the elevator and aileron was done to capture the control surface commands. The results from the studies are shown below in FIGURE 58.

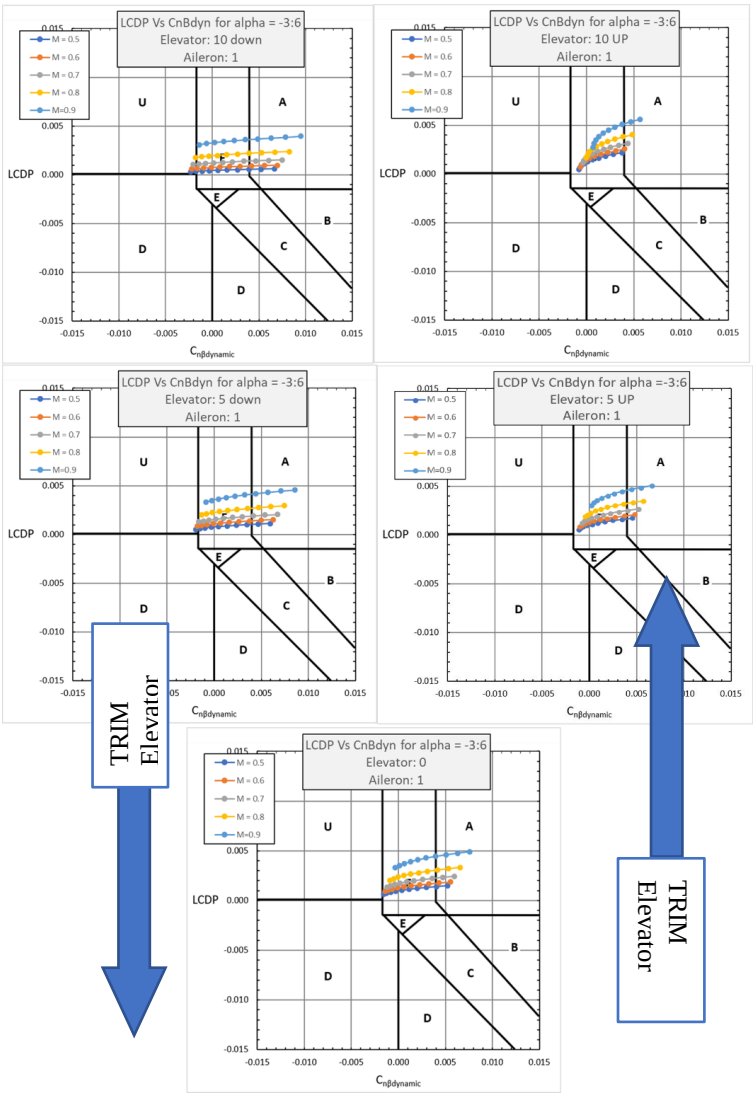

FIGURE 58. Evolved-Bihrle-Weissman Plot of Shuttle Orbiter – Subsonic data from VORLAX examining the effect of collective elevon trim on both $Cn_{\beta DYN}$ and *LCDP*.

The studies below only show how collective elevon "elevator trim" impacts *LCDP* and $Cn_{\beta DYN}$. We can conclude from these studies that moving from collective elevon angles from "elevator down" to "elevator up" shortened the range of $Cn_{\beta DYN.}$ Whereas in the max "elevator down" position, α of 10^{o} and Mach of 0.9, $Cn_{\beta DYN}$ ranged from -0.002 to 0.009, when elevator was upward position at the same angle and

Mach Number, the range shrunk to be between 0.0 to 0.007. With the corresponding *LCDP* values for the α of 10° and Mach of 0.9 case, *LCDP* ranged from 0.003 to 0.0045. In the upward position, the range grew to be between 0.003 to 0.0052. This analysis proved meaningful in determining some key trends when trying to validate the VORLAX model to the flight results. It also illustrates that for elevon style control surfaces, lateral-directional and longitudinal stability are somewhat coupled.

To further validate that the VORLAX model was an accurate indicator of Shuttle stability, we made a comparison to the flight data. For the control points that used the subsonic and supersonic portion of the flight, those being the Mach 0.7 at α of 4° and Mach 2 at α of 12° the data aligned semi accurately from VORLAX. The elevator setting was positive 5° upward and differential aileron deflection of 3°. These deflections prove to be relatively close to reported NASA deflections as seen in FIGURE 59 [17].

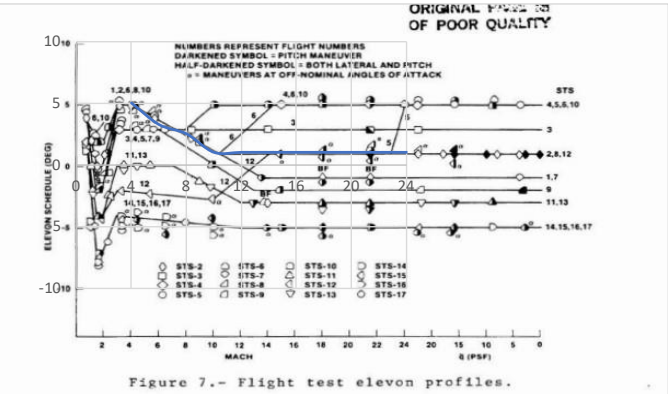

FIGURE 59. Orbiter Collective Elevon Deflection "Elevator" Schedule [17].

It is hard to judge which control surface deflections were used below Mach 2 as seen in the FIGURE 59 with the clutter. Likewise, the values for the *LCDP* and $Cn_{\beta DYN}$ could not be determined below Mach 2 as the graphs do not fall below that value. (See FIGURE 13 through FIGURE 17) But for the values used, it is not unreasonable as it does correspond to the elevator schedule. For the Mach 2 control point, the central body flap was deflected 45 degrees.

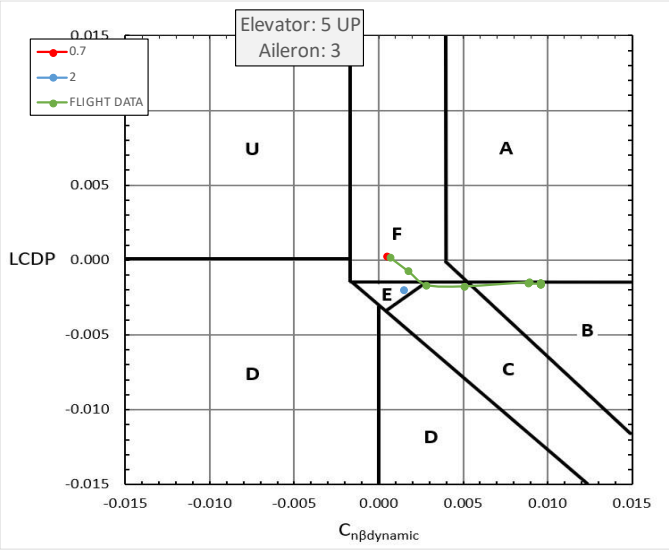

FIGURE 60. Evolved-Bihrle-Weissman Plot of Shuttle - VORLAX in comparison to Flight Test Data.

FIGURE 60 illustrates the accuracy of the model to the flight data. We see that the first point, the red point, is fairly close to the first point in the flight data. This similar result helps to validate VORLAX's accuracy. The second control point, the blue point, is more off than the previous point. It is off in the $Cn_{\beta DYN}$ value but close in *LCDP* value. The difference in the VORLAX to the flight data is attributed to the various other control surfaces. It was noted that at lower Mach numbers the split flap would deploy throughout the trajectory. Being able to determine what the setting was proved to be difficult as the input was pilot controlled for Mach 2 below and was used

to help align for final approach. The split flap schedule for the flight trajectory did have data for below Mach 2 but has it as a single value. When watching reentry film for STS-129, We see that around Mach 2, the body flap, and elevators are trimmed upward, matching the control points in VORLAX, but we see that the vertical stabilizer split flap is also deployed but varies in deployment all the way down to final. See FIGURE 61. for the split flap deployed around Mach 2. This image is taken from a NASA YouTube video of a shuttle landing and is found around the 1:27 minute mark [46].

FIGURE 61. Elevator Up and Split Rudder "Speed Brake" Deployed at Mach 2.

One of the key features that could not be modelled by VORLAX was the split rudder "speed brake." Due to the inability to represent the split rudder flap confidently in VORLAX, the difference between the flight data and the results were considered close enough. With both the results from the subsonic and supersonic model being reasonably close, it could be determined that the Bihrle-Weismann is accurate in matching the flight test data to simulated model data.

In trying to determine why the Mach 2 control point was not as accurate as the Mach 0.7 control point, a trade was conducted varying the body flap. This was done because the Mach of 0.7 control point had no body flap deflection while matching the surface deflection and was accurate to the flight data while the higher Mach number which had accurate deflections was lacking. The body flap outside of the split flap, was the only surface not deflected. A run with the body flap deflected at 10 degrees up vs. 45 degrees up is shown in FIGURE 62. We see that by varying the body flap has an impact on the $Cn_{\beta DYN}$. It results in a more negative value for $Cn_{\beta DYN}$; this indicates that a pitch-plane maneuver can effectively destabilize a vehicle in yaw.

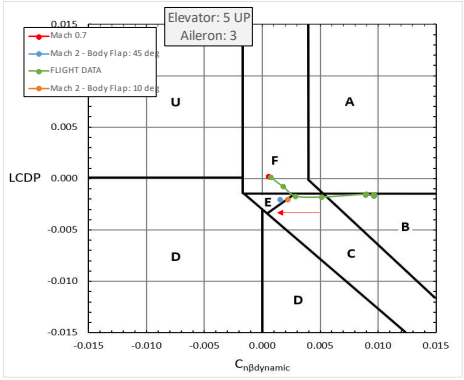

FIGURE 62. VORLAX Body Flap movement impacts on the Evolved-Bihrle-Weissman Plot.

The results found in VORLAX for the subsonic model helped to provide accuracy and confidence in the computational aerodynamic database that would be used in designing alternative configurations of the shuttle. It also showed that there is an effect on elevator and body flap trim on *LCDP* and $Cn_{\beta DYN}$. However, we can also conclude through examination of the flight data, aerodynamic model, and the results of history itself that combinations of elevator, aileron, and body flap deflections can control the vehicle, albeit in a limited manner.

COMPUTATIONAL STUDY OF VARIOUS SHUTTLE CONFIGURATIONS

Tip Dihedral Study

For the various configurations of the shuttle, the designs incorporated the additions of tip verticals. The initial considerations analyzed the effect of the angle of tip dihedral of the tip vertical. This was done in order to determine whether there was an optimal angle for increasing the *LCDP* and $Cn_{\beta DYN}$; see FIGURE 63.

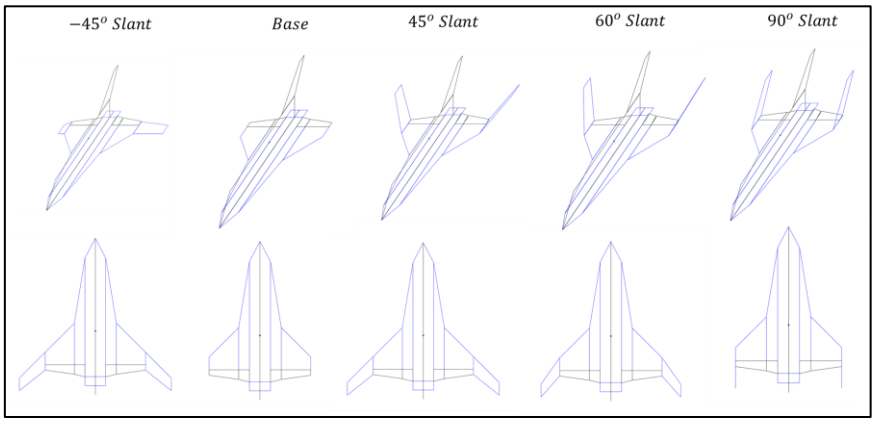

FIGURE 63. Various VORLAX models.

The first design of various models that was developed was the tip dihedral of 45^o. This design added a tip vertical that extended at a 45^o upward tip dihedral, adding an extra 20 feet outboard and 20 feet vertical. Its leading-edge angle maintained the leading-edge sweep of the wing [39]. That being 45^o wing sweep leading into the wing tip vertical sweep. The additional wing tip verticals increased the overall wingspan and wing reference area. The changes in wingspan and reference area are shown in TABLE 3.

Model	Sref (ft^2)	Wingspan (ft)
Base	2690	78.1
(-)45 Degree	3160	118
45 Degree	3160	118
60 Degree	3022	106
90 Degree	2690	78.1

TABLE 3. Wing Reference Area and Wingspan Changes.

For the various other configurations, those being the -45, 60, and 90-degree tip dihedrals, the leading-edge sweep and basic areas added for 45-degree model were maintained throughout. This was done by maintaining the leading-edge length of $20\sqrt{2}$ feet. Again, the leading-edge length was determined by the vertical tip extending an extra 20 feet outward and upward at 45^o. The only difference was the tip dihedral angle; refer to FIGURE 63.

Because CG impacts the vehicles stability, a separate analysis for CG location was conducted post dihedral study. This was done post dihedral study because of the lack of the ability to accurately determine the additional weight of the tip verticals. Furthermore, the addition of the tip verticals will indeed change the mass moments of inertia for the vehicle. That likewise was hard to estimate and held constant for the subsequent study. This is important due to the impact that the mass moments of inertia have on the $Cn_{\beta DYN}$. See equation (1) below.

$$Cn_{\beta DYN} = \frac{dCn}{d\beta} * cos(\alpha) - \frac{dCl}{d\,\beta}\left(\frac{I_{zz}}{I_{xx}}\right) * sin(\alpha) \quad (1)$$

The mass moment of inertia ratio is a leading coefficient to the rolling moment due to side slip term ($dC_l/d\beta$). If the desired result in the Bihrle-Weissman chart is to reside in the stable region "A," then $Cn_{\beta DYN}$ must be positive. One way that that is possible is for the rolling moment due to side slip term ($dC_l/d\beta$) to be negative thus resulting in the addition of the second term. Of course, the angle of attack (α) could cause a sign change, but generally speaking, if the angle of attack (α) is positive and rolling moment due to side slip term ($dC_l/d\beta$) is negative, then mass moment of inertia ratio could be considered benign. Therefore, the moments of inertia are held constant to the original shuttle configuration as long as the resulting rolling moments are negative through the same angles of attack as the yawing moment coefficient is positive. This was verified post Bihrle-Weissman analysis to check stability in all planes. The impact of tip dihedral angle on *LCDP* and $Cn_{\beta DYN}$ can be seen in FIGURE 64.

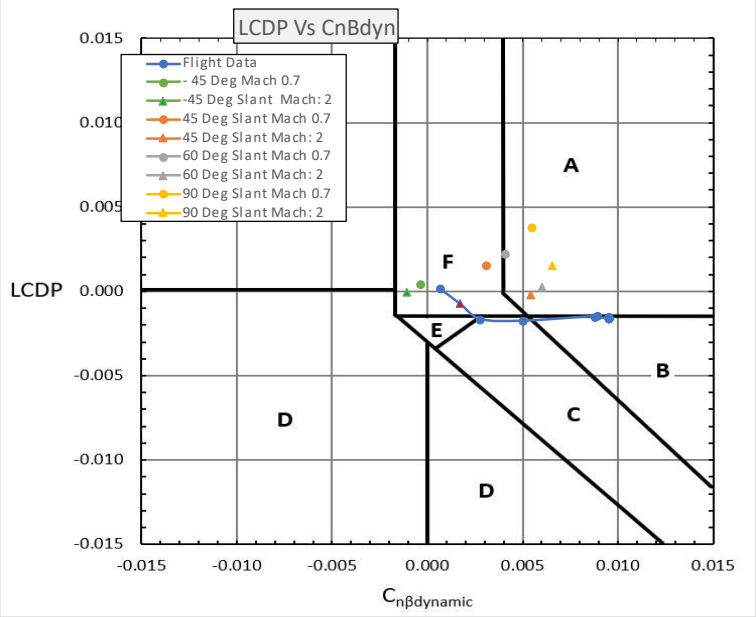

FIGURE 64. Evolved Bihrle-Weissman for Various Tip dihedral

We see from the Evolved-Bihrle-Weissman Chart (FIGURE 64 Below) that as the angle of the tip dihedral increases, the stability of the vehicle increases in the Region A. This would indicate that the vehicle goes from a weak departure and spin resistance to a very strong departure and spin resistance. The 90-degree tip dihedral did best.

It is also seen that from the Mach 0.7 condition, the circles in FIGURE 64, compared to the Mach 2 condition, the triangles, that the stability moves across the chart in almost a diagonal direction South-East. The drop and movement in relative *LCDP* and $Cn_{\beta DYN}$ values for the increase in Mach number indicate that stability is indeed influenced by speed. This is further illustrated in FIGURE 65 and FIGURE 66 when comparing the impact of these values to the relationship of Mach Number

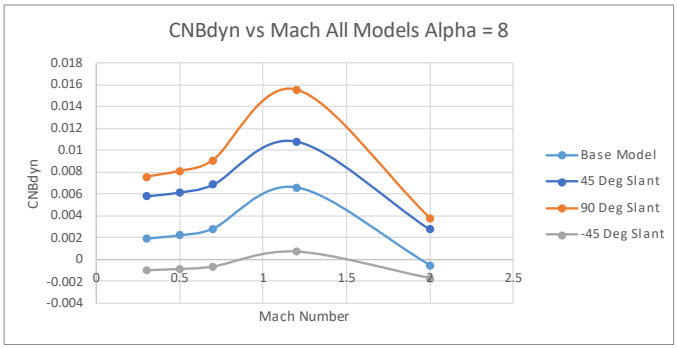

FIGURE 65. $Cn_{\beta DYN}$ *vs* Mach for Different Wing Tip Dihedral.

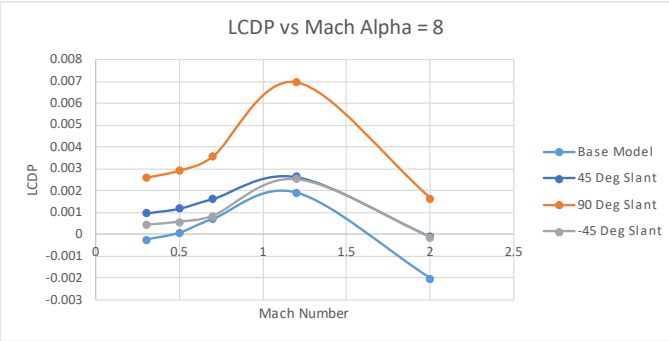

FIGURE 66. LCDP vs Mach for Different Wing Tip dihedrals.

We see that *LCDP* and $Cn_{\beta DYN}$ share a similar trend when compared to the increase in Mach number. They both gradually increase over a small subsonic range, then increase more dramatically and peak around optimal Mach number then begin to precipitously drop off. This would indicate an optimal configuration and optimal speed. The precipitous drop off as the vehicle surpasses the peak Mach number would further indicate the destabilizing nature of increasing Mach number. That pass a certain point, the quality and quantity of stability both drop off quickly. This would further hint at a need for a healthy amount of stability is needed in a hypersonic environment as it will tend to become very destabilizing.

The impact of angle of attack alpha on *LCDP* and $Cn_{\beta DYN}$ for the tip dihedral configurations is seen in this FIGURE 67 and FIGURE 68 below .

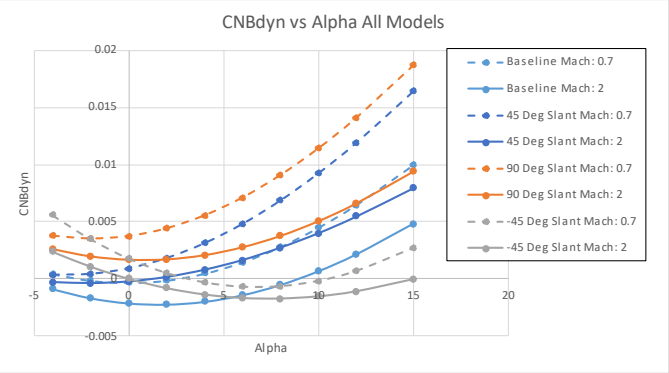

FIGURE 67.$Cn_{\beta DYN}$ vs Alpha for Different Wing Tip dihedral.

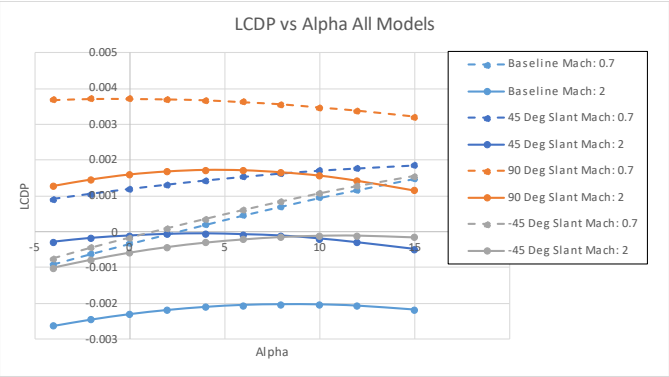

FIGURE 68. LCDP vs Alpha Different Wing Tip dihedral.

Alpha seems to have a greater impact on $Cn_{\beta DYN}$ than *LCDP*. In FIGURE 65. We see that it grows rather quickly at the lower Mach number as alpha increases. At the higher Mach number, Mach 2 $Cn_{\beta DYN}$ continues to increase as alpha increases. This shows that angle of attack has a positive impact on stabilizing effects. Whereas the *LCDP* seems to be affected with a shallow drop-off in value as alpha increases at higher Mach values. It contrasts with the lower Mach number cases; these have *LCDP* increasing as alpha increases.

Overall, for all the configurations, the 90-degree tip dihedral proved best for the subsonic to supersonic flight regime. For a similar size wing extension, it firmly planted the newly configured shuttle in Region "A" of the Evolved-Bihrle-Weissman. (See FIGURE 24.) The 90-degree tip dihedral further proved that it has the highest values of *LCDP* and $Cn_{\beta DYN}$ through the various Mach numbers and alphas as seen in FIGURE 67 through FIGURE 68. Knowing how *LCDP* and $Cn_{\beta DYN}$ are influenced by the Mach number and angle of attack, that being the overall decrease in effectiveness as Mach number increases would indicate that for the hypersonic flight regime, a configuration that firmly locates the shuttle in Region "A" would be necessary.

Wing Tip Vertical Sizing Study

At the conclusion of the tip dihedral study, we saw that the 90-degree options proved to be the best option. A further study was conducted in order to see the impact of the size of tip vertical. Three different sizes were decided. Those being a small, medium, and large. For the three sizes, unlike the wing tip dihedral which maintained the leading-edge sweep from the wing-to-wing tip vertical, the leading edge for the tip vertical was not maintained. The key variable for this study was the impact of the height. The small size had a height of 15 feet, the medium was the 90-tip dihedral height of 28.2 feet and the largest had a height of 35 feet. Because the 90 deg tip dihedral did not extend outward, the wingspan and reference area were the same as the base model. Those being the wingspan of 78.1 feet and wing reference area of 2690 square feet. See FIGURE 69. For the sizes.

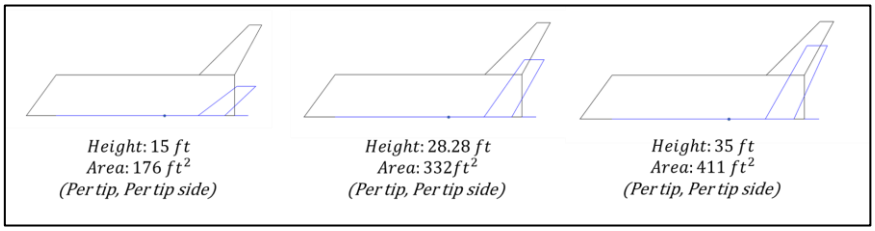

FIGURE 69. Wing Tip Vertical Sizes.

When plotting the comparison of the small, medium, and large configurations on the Evolved-Bihrle Weissman, as seen in FIGURE 70, it is clear that the large vertical wing tips did the best at moving the resulting *LCDP* and $Cn_{\beta DYN}$ values into the "A" Region of the chart. It is also similar to the results of the tip dihedral studies in that the higher Mach number, Mach 2, has shown an appreciable drop from the subsonic case.

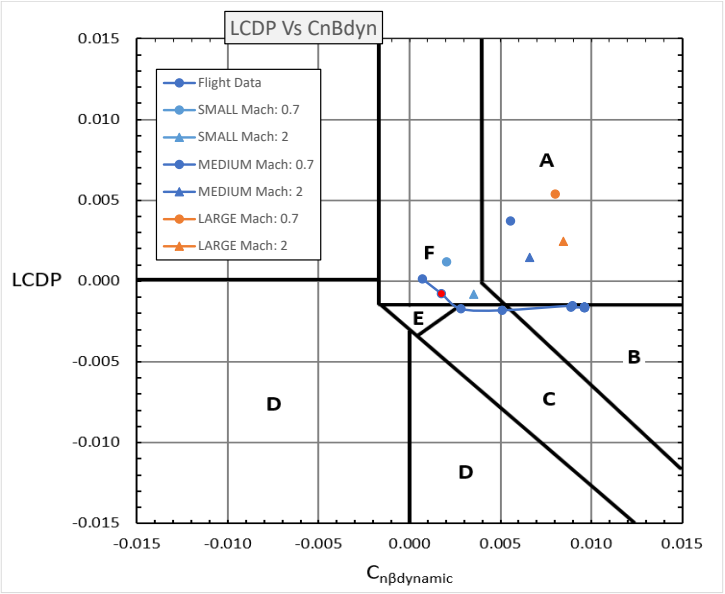

FIGURE 70. Evolved Bihrle-Weissman for Various Wing Tip Fin Sizes.

Similar to the wing tip dihedral study, the trends for the $Cn_{\beta DYN}$ vs. Mach number and *LCDP* vs. Mach number trend similarly. They even match the tip dihedral study in trend. The similarities in trend extend to the comparisons of wing tip vertical sizes and the impact of angle of attack.

There a key similarity is seen in the angle of attack response. That for $Cn_{\beta DYN}$ vs. alpha, FIGURE 67 and FIGURE 73, the subsonic condition is nominally greater than the supersonic condition. This key similarity is contrasted by another key difference. Comparing the type of response for FIGURE 74 to FIGURE 68, We see that the supersonic case is nominally greater than the subsonic case in FIGURE 74 whereas the contrary is seen FIGURE 68.

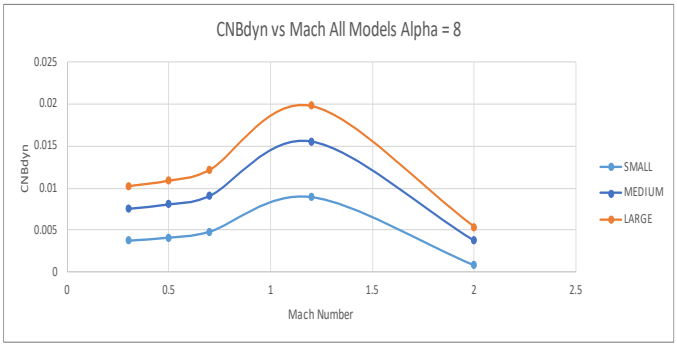

FIGURE 71. Mach vs $Cn_{\beta DYN}$ Different Wing Tip Sizes.

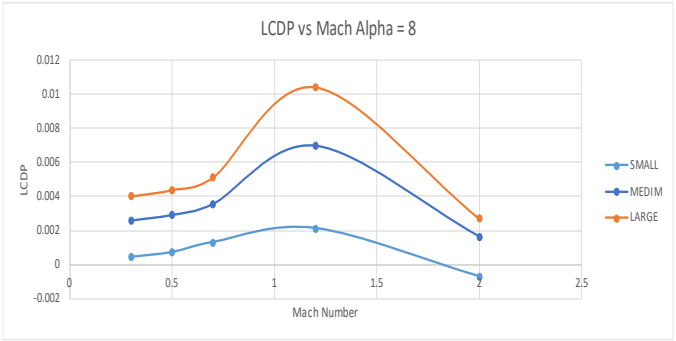

FIGURE 72. Mach vs LCDP for Different Wing Tip Sizes.

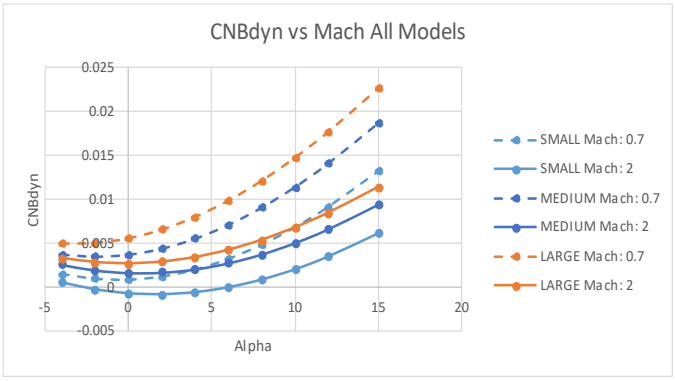

FIGURE 73. $Cn_{\beta DYN}$ vs Alpha for Different Wing Tip Sizes.

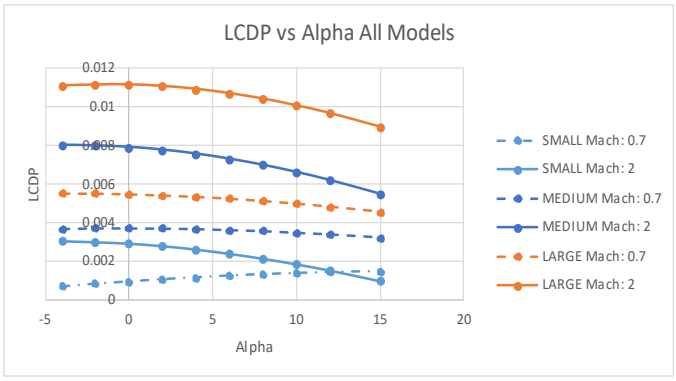

FIGURE 74. Alpha vs LCDP for Different Wing Tip Sizes.

At the present time we can compare FIGURE 68 (the tip dihedral study) to the FIGURE 74 (wing tip fin size study). We see that fairly large tip fins are needed to clean up the aerodynamic controllability at subsonic through supersonic speeds.

Hypersonic Study

The shuttle on reentry had a hypersonic flight regime from Mach 26 down to Mach 4 and below. For this analysis, the flight regime under consideration will only span Mach 2 to Mach 6. VORLAX's accuracy for lateral-directional stability was shown to be within reason for up to Mach 5 when compared to the flight test data. The hypersonic flight regime under study was expanded to Mach 6 to capture at least one

more control point in the shuttle's flight trajectory. Please refer to the section "V. Computational Study of Baseline Shuttle Lateral-Directional Controllability" above to see the accuracy of VORLAX at hypersonic speeds.

From the tip dihedral study and the wing tip fin size study, the hypersonic study will analyze what was considered best configuration for subsonic/supersonic performance. It was shown that the 90 deg slant performed best and improving the lateral- directional stability. It was further seen that from varying sizes, that the largest vertical tip did best. For the hypersonic portion of the study, it will resume here in comparing the sizes of the tip verticals. For the hypersonic analysis Mach numbers from 2,3,4,5, and 6 were considered. A range of angles of attack (α) were utilized from -4, -2, 0, 4, 6, 8, 10, 15, 20, and 30.

FIGURE 75 shows the comparison of the wing tip vertical sizes to the Evolved Bihrle-Weissman at Mach 4 and Mach 6. We see that the hypersonic speed FIGURE 75 compared to the subsonic/supersonic FIGURE 70, that there is a significant drop in LCDP. Even between Mach 4 and Mach 6, the drop is substantial. However, it can be noticed that all tip verticals remain in the "A" region and stay stable, but they are descending and approaching the "B" region as speed increases.

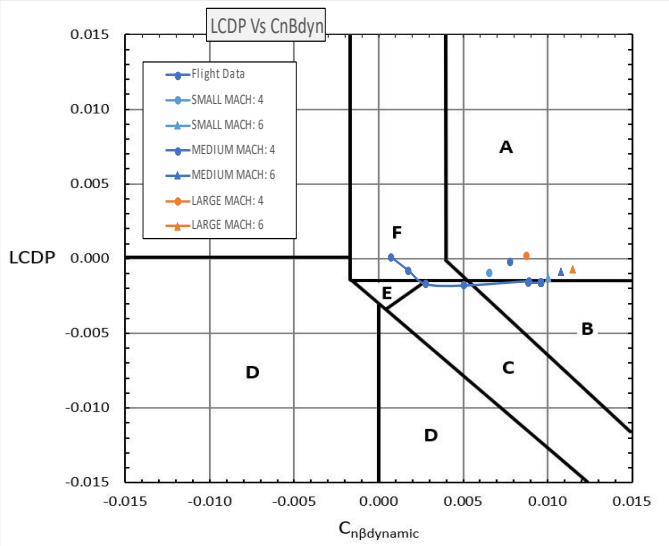

FIGURE 75. Evolved Bihrle Weissman Mach 4 & Mach 6.

Similar to the subsonic studies, we see that the LCDP and $C_{N\beta dyn}$ versus alpha in FIGURE 78 and FIGURE 79 trend the same yet at greatly diminished values. Versus Mach number in FIGURE 76 and FIGURE 77 it does not trend similarly. The LCDP and $C_{N\beta dyn}$ get small and approach a minimum value as Mach increases.

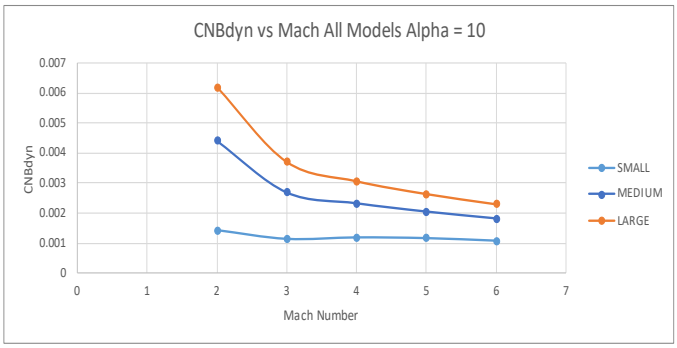

FIGURE 76. Hypersonic Mach vs $Cn_{\beta DYN}$ Different Wing Tip Fin Sizes.

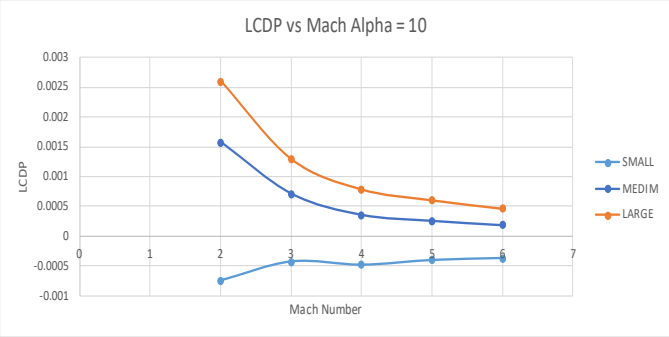

FIGURE 77. Hypersonic Mach vs LCDP for Different Wing Tip Sizes.

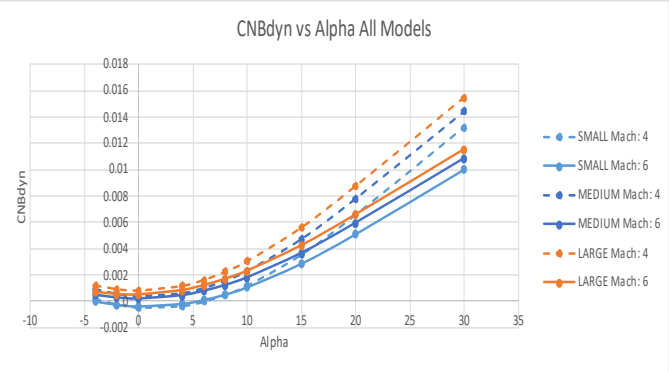

FIGURE 78. Hypersonic $Cn_{\beta DYN}$ vs Alpha for Different Wing Tip Fin Sizes.

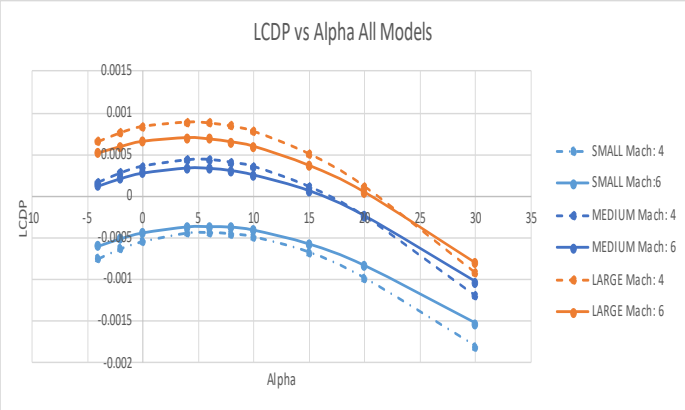

FIGURE 79. Hypersonic Alpha vs LCDP for Different Wing Tip Sizes.

Therefore, with the results from the Bihrle-Weissman in FIGURE 75 showing the vehicle in the "A" region and most firmly in "A" at the largest tip verticals, the modified shuttle with 90-degree tip verticals would be best for enhancing stability of the vehicle. Plotting the response of the vehicle in yaw, pitch, and roll to assess its handling qualities illustrate how too much of a good thing can become detrimental.

We see that in FIGURE 80 and FIGURE 81 for roll and yaw respectively the vehicle is stable. We see that for rolling moment (C_l) becomes negative and helps to maintain stability while yawing moment (C_n) is increasing and maintaining the weathercock stability. However, FIGURE 82 for pitch stability (C_m) at Mach 4 the vehicle looks stable and increases as lift coefficient increases but at Mach 6 becomes unstable. It would seem to reverse in its entirety. Therefore, although the 90-degree tip verticals help to increase the stability of the vehicle, are they the best for hypersonic flight?

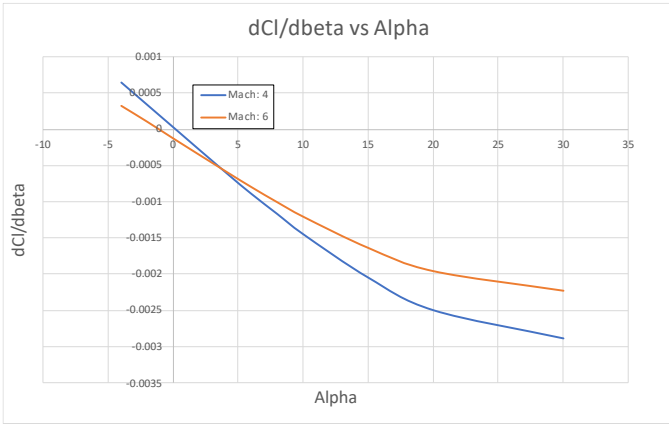

FIGURE 80. $dC_l/d\beta\ vs\ \alpha$ Large 90-deg.

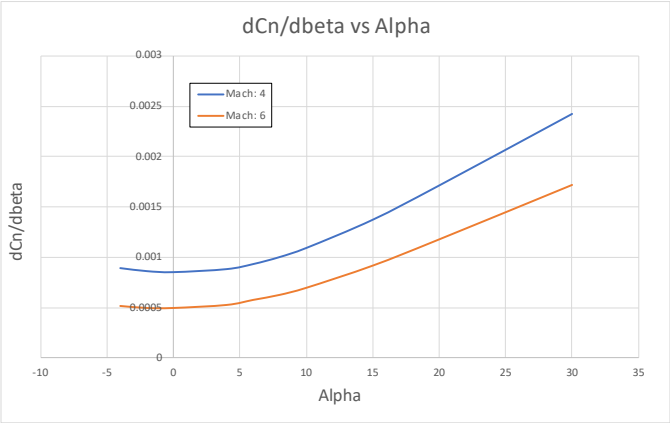

FIGURE 81. $dC_n/d\beta \; vs \; \alpha$ Large 90-deg.

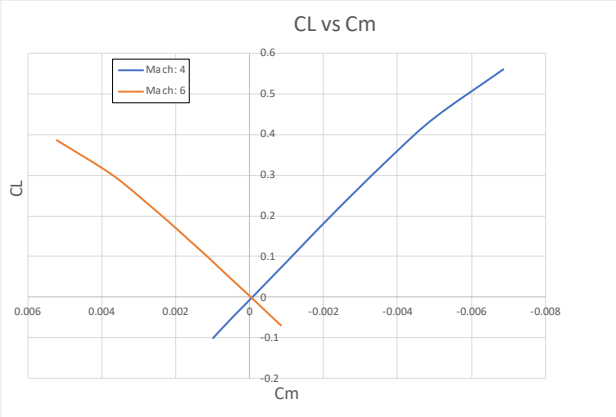

FIGURE 82. $C_L \; vs \; C_m$ Large 90-deg.

The 45, 60, and 90 slant study was therefore conducted again. Knowing however that size indeed impacts the stability of the vehicle, it would not be considered for this review. The original sizes of the slanted wing tips were used and analyzed at hypersonic speeds. Furthermore, because Mach 6 and presumably higher seems to reverse in its entirety, a comparison at Mach 6 seemed sufficient to illustrate the following point. FIGURE 83 through FIGURE 85 show the results of the re-run slant wing tip verticals at hypersonic speeds.

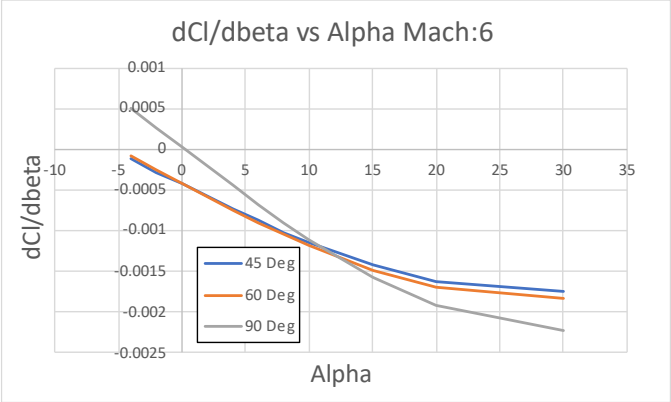

FIGURE 83. $dC_l/d\beta \; vs \; \alpha$ 60-deg.

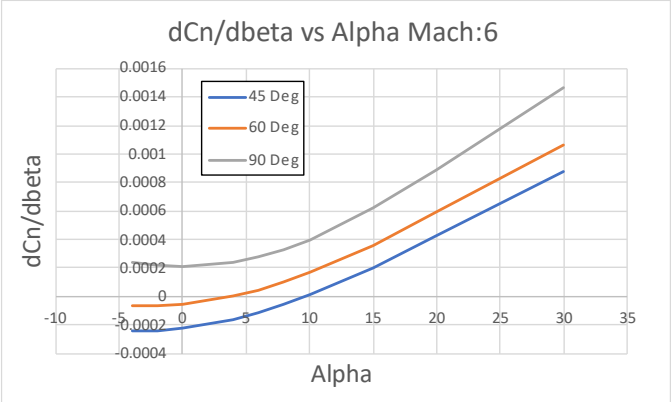

FIGURE 84. $dC_n/d\beta \; vs \; \alpha$ 60-deg.

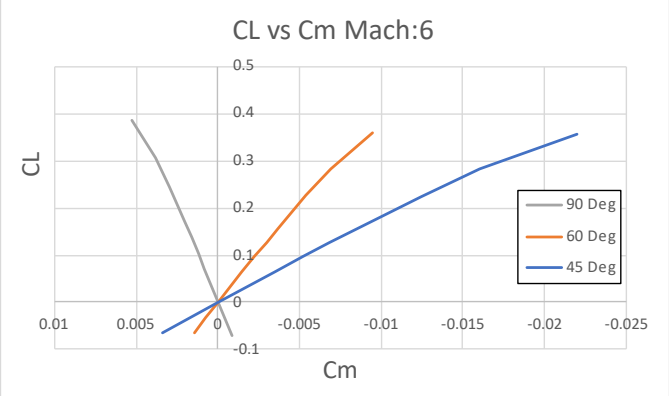

FIGURE 85. $C_L \; vs \; C_m$ 60-deg.

We see in the FIGURE 83 and FIGURE 84 that the all the wing tip configurations are stable in yaw and roll. However, in FIGURE 85 for pitch, we see that the 90 degrees falls out. We see that 60 degrees is stable for yaw, pitch, and roll. When plotted into the evolved Bihrle-Weissman, FIGURE 86, the 60^{o} dihedral tip fin is more firmly in the "A" region than the 45^{o} dihedral tip fin.

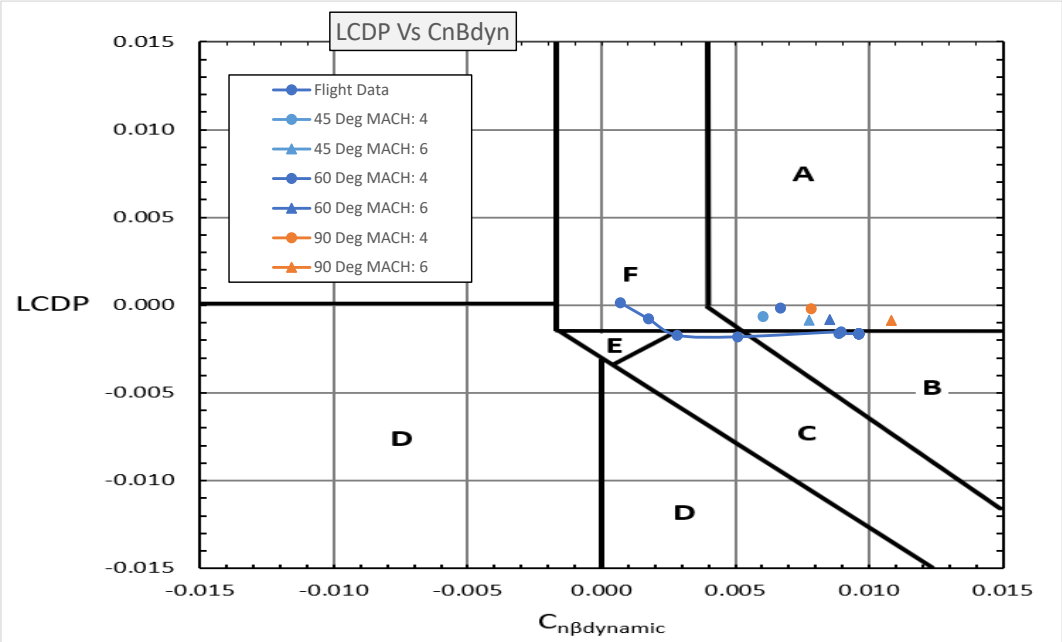

FIGURE 86. Evolved Bihrle-Weissman Wing Tip Slant Comparison at Hypersonic Mach Numbers.

Center of Gravity Impact

For all the configurations of the wing tip studies, it was assumed that the center of gravity would be in the same location of the original vehicle. That location being 71.40 feet [42] from the nose of the shuttle. This assumption was in some ways a bit presumptuous due to additional mass being added to the vehicle without relocation of the center of gravity. Therefore, it was incumbent on us to analyze how movement of the center of gravity (CG) would affect the stability of the vehicle in the new configuration. For the analysis, the configuration under consideration was the finalized 60-degree wing tips. The center of gravity was moved forward of the original location and moved aft of the original location. Moving the center of gravity aft would make the most sense due to the additional tips being added aft of the original center of gravity. The distances varied from 65.40, 68.40, 71.40, 72.40, 73.40, 76.40, 79.40, and 82.40 feet. These lengths resulted in CG movement from 60.6% to 76.3%. The original location of 71.40 feet was at 66.1%. See FIGURE 87 through FIGURES 95 below.

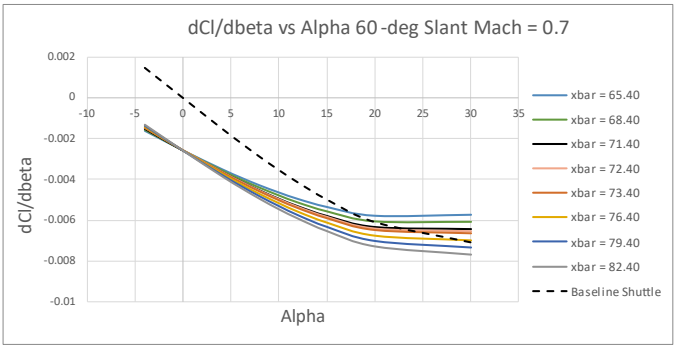

FIGURE 87. $dC_l/d\beta \; vs \; \alpha$ Subsonic 60-Deg.

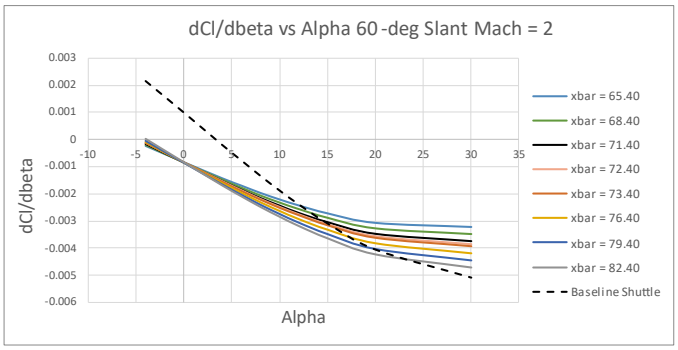

FIGURE 88. $dC_l/d\beta \; vs \; \alpha$ Supersonic 60-Deg.

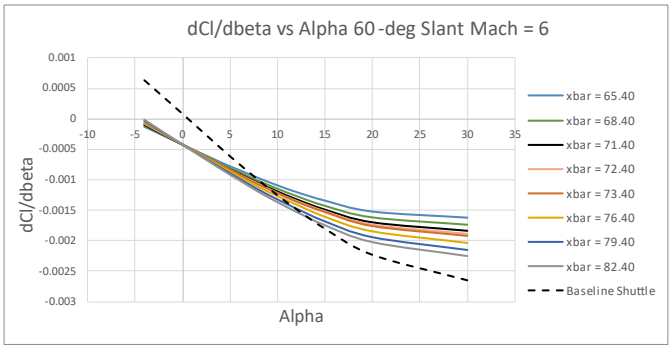

FIGURE 89. $dC_l/d\beta \; vs \; \alpha$ Hypersonic.

The rolling moment due to sideslip ($dC_l/d\beta$) versus angle of attack (α) graphs, FIGURES 87 through FIGURE 89, indicate that the vehicle remains stable in roll at sideslip through all angles of attack. The overall magnitude of the response becomes smaller. This is seen in the values ranging from -0.002 to -0.008 at the subsonic speed to -0.0005 to -0.0023. The variance in CG becomes more distinguished at high angles of attack, around 15 to 30 degrees, yet does little to destabilize.

In the yaw plane, FIGURES 90 through 92, we can see that moving the CG forward and aft shifts the overall trend of the yawing moment due to sideslip. Going from subsonic to supersonic and up to hypersonic, it can be noted that the overall magnitude of the yawing moment response diminishes and becomes smaller, similar to the rolling moment. Unlike the rolling moment above, where smaller ranges of response did not destabilize the vehicle in that plane, the yawing moment becomes more unstable as the speed increases. At subsonic speed, FIGURE 90, where CG of 76.40 feet is still stable, at hypersonic speed, FIGURE 92, that same CG location is only stable at high angles of attack (>15 degree). Only CG's less than the original location of 71.40 feet are stable through all flight regimes and all angles of attack.

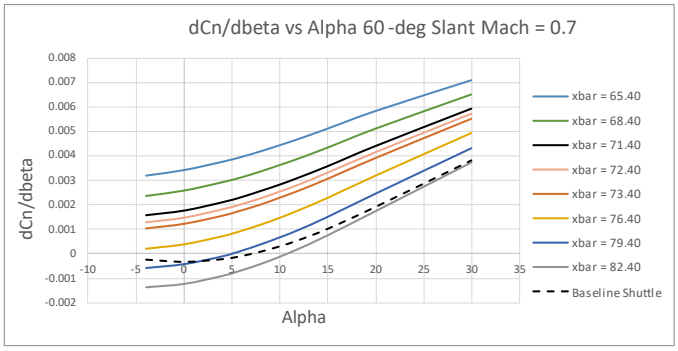

FIGURE 90. $dC_n/d\beta \; vs \; \alpha$ Subsonic 60-Deg.

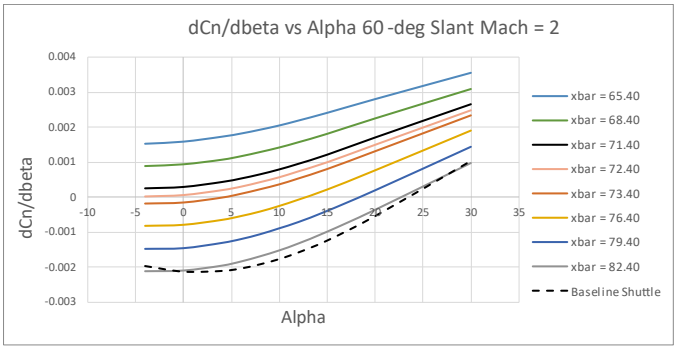

FIGURE 91. $dC_n/d\beta \; vs \; \alpha$ Supersonic 60-Deg.

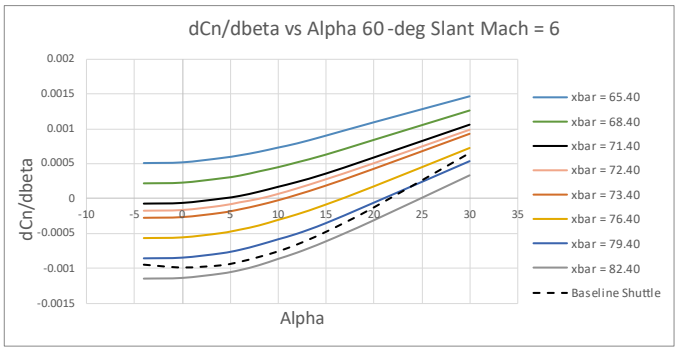

FIGURE 92. $dC_n/d\beta \; vs \; \alpha$ Hypersonic 60-Deg.

For the subsonic case, FIGURE 93, it is seen that the moving the CG from 65.40 feet to 76.40 feet keeps the vehicle stable in pitch. Going supersonic, the same range is still stable. However, at hypersonic speeds, FIGURE 95, moving the CG aft destabilizes the vehicle. Moving the CG just one foot aft puts the vehicle in an unstable pitch. Therefore, in the pitch plane, aft movement on the CG would not be suitable due to the limiting case at hypersonic speeds. It is also concluded that the addition of the wing tip verticals should not move the CG outside the original shuttle location.

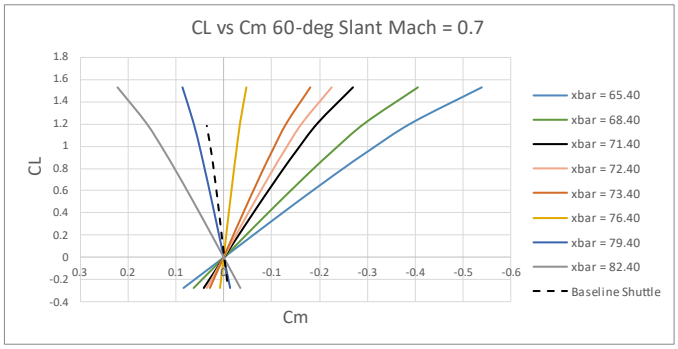

FIGURE 93. $C_L \; vs \; C_m \; CG \; Subsonic$ 60-Deg.

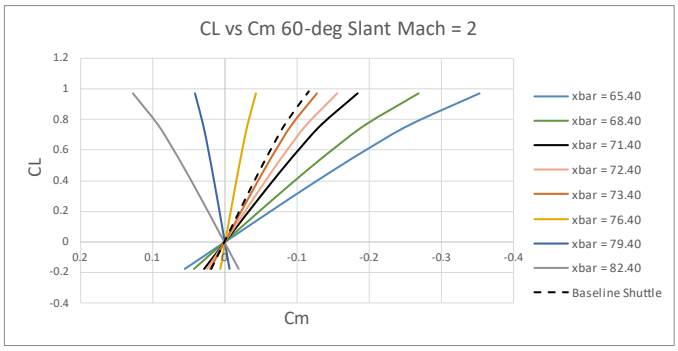

FIGURE 94. C_L *vs* C_m *CG Supersonic* 60-Deg.

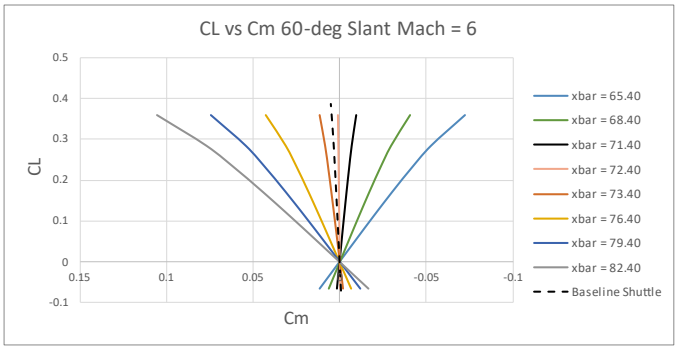

FIGURE 95. C_L *vs* C_m *CG Hypersonic* 60-Deg.

The 60-degree slanted verticals are the best choice for improving the subsonic, supersonic, and hypersonic stability of the space shuttle. They improve the vehicle and make it not as reliant on the RCS thrusters. It could be safely presumed as it was concluded above that increasing the size of the tip verticals would make them better. The final trajectory on the evolved Bihrle-Weissman is shown in FIGURE 96.

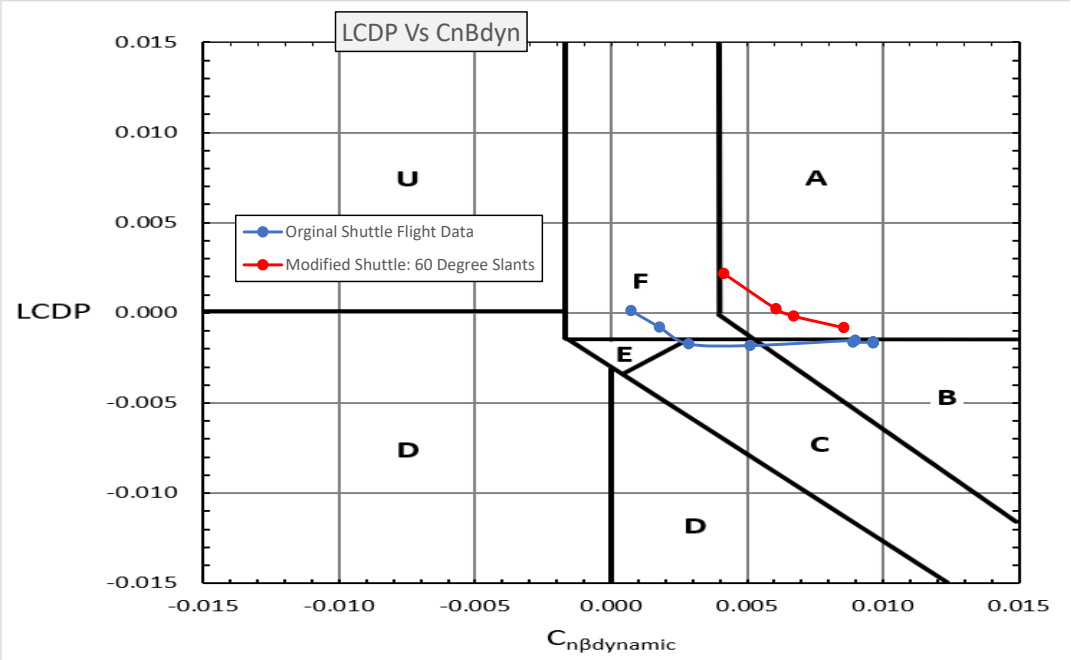

FIGURE 96. Evolved Bihrle-Weissman for Final Modified Shuttle with 60-Deg Slanted Wing Tips.

CONCLUSION

This thesis shows that the NASA Shuttle Orbiter design had issues with stability which required active control using RCS to compensate for inherent aerodynamic control problems due to the flight regime and its demands. It further shows that the because of its multi-regime flight envelope, trade-offs were made to maintain control.

The first insight obtained from this thesis is that these problems are not specifically hypersonic issues, as they are seen across the entire flight envelope from subsonic, through supersonic, to hypersonic, and from moderate to high angles of attack. The degraded roll and yaw stability at high speed and high angles of attack was acceptable because pitch command was more critical due to the need for aerobraking. However, due to design these could have been modified or corrected. This is illustrated by the wing tip vertical studies. They concluded that the addition of slanted 60-degree wing tip verticals were sufficient to aerodynamically stabilize the vehicle without any need of RCS thruster. Notwithstanding, the slight over predictability of VORLAX, the results match flight data well and show that the modifications in VORLAX are accurate, even in low hypersonic for lateral-directional necessities. Although the modifications shown herein were sufficient in improving stability, designers at the time may have had to make tradeoffs for the vehicle development when the potential improvements may not have been great enough to justify entirely new sets of wing tips.

The second major insight is that there are obvious aerodynamic cross coupling effects seen on a vehicle where elevons are used collectively for "elevator" trim and differentially for "aileron" command. In the case of the shuttle, the choice of collective elevon deflection can be altered through use of both a central "body flap" and a split-rudder "speed-brake." The thesis shows that elevator effects are more than secondary in regard to the lateral-directional stability of the vehicle and that longitudinal trim maneuvers do indeed affect the lateral-directional stability.

REFERENCES

1. See: https://www.nasa.gov/centers/dryden/history/pastprojects/HyperX/index.html (accessed Nov. 7, 2022)

2. See: https://www.nasa.gov/topics/aeronautics/features/X-51A.html (accessed Nov. 7, 2022)

3. Jenkins, D.R. and Landis, T.R., Hypersonic: The Story of the North American X-15, Specialty Press, North Branch, MN, 2003.

4. Anon. “Proceedings of the X-15 First Flight 30th Anniversary Celebration.” NASA CP-3105, 1989.

5. Arrington, J.P. and Jones, J.J., ed., "Shuttle Performance: Lessons Learned," NASA CP 2283 Part 1, 1983.

6. Kay, W.D. “The X-15 Hypersonic Flight Research Program: Politics and Permutations at NASA,” NASA SP-4219, NASA, Washington, D.C., 1998. See: https://history.nasa.gov/SP-4219/Chapter6.html (accessed Nov. 7, 2022)

7. Jenkins, D.R., Space Shuttle: The History of Developing the National Space Transportation System, Walsworth Publishing, Marceline, MO, 1997.

8. Bertin, J.J., Hypersonic Aerothermodynamics, AIAA, 1993.

9. Philips, W.H., "Effect of Steady Rolling on Longitudinal and Directional Stability," NACA TN-1627, 1948.

10. O’Brien, K.P. and Takahashi, T.T., “An Investigation of the Bell X-2 and the Factors that Led to Its Fatal Accident,” AIAA 2022-3203, 2022.

11. Takahashi, T.T., “Maneuvering Capabilities of Hypersonic Airframes,” Accepted for publication at the 2023 AIAA SciTech Meeting, January 2023.

12. Griffin, J.A. and Takahashi, T.T., “Hypersonic Aircraft Performance Limitations Arising from Aerodynamic Control Limits,” Accepted for publication at the 2023 AIAA SciTech Meeting, January 2023.

13. Griffin, J. A. and Takahashi, T.T., “Aero-Spaceplane Mission Performance Estimations Incorporating Atmospheric Control Limits,” AIAA 2022-3656, 2022.

14. Mason, W.H., "High Angle-of-attack Aerodynamics" see: http://www.dept.aoe.vt.edu/~mason/Mason/AeroHighAlpha.html

15. Scheiss, J.R., “Lateral Stability and Control Derivatives Extracted from Space Shuttle Challenger Flight Data,” N88-16788, NASA TM 100520, January 1988.

16. Stone, J.S., Baumbach, J.J. and Roberts, B.B., “Space Shuttle Orbiter Reaction Control Subsystem Flight Data Anomalies,” NASA CP 2283 Part I, 1983.

17. Cooke, D.R., “Minimum Testing of the Space Shuttle Orbiter”, NASA N84 10134, 1983

18. Seltzer, R.M. and Rhodeside, G.R. “Fundamentals and Methods of High-Angle-of-Attack Flying Qualities,” Office of Naval Technology AD-A2359 94, January 1988

19. Weissman, R., "Status of Design Criteria for Predicting Departure Characteristics and Spin Susceptibility," AIAA 74-791, 1974.

20. Weissman. R., "Preliminary Criteria for Predicting Departure Characteristics' Spin Susceptibility of Fighter-Type Aircraft," AIAA Journal of Aircraft, Vol. 10, No. 4, April 1973.

21. Takahashi, T.T., Aircraft Performance and Sizing, Volume II: Applied Aerodynamic Design, Momentum Press, New York, 2016.

22. Day, R.E., "Coupling Dynamics in Aircraft Design: A Historical Perspective," NASA SP-532, NASA, 1997.

23. Takahashi, T.T., Griffin, J.A. and Grandhi, R.V., “A Review of High-Speed Aircraft Stability and Control Challenges,” submitted for review and potential publication at AIAA Aviation 2023.

24. Skow, A.M. and Titiriga, A., "A Survey of Analytical and Experimental Techniques to Predict Aircraft Dynamic Characteristics at High Angles of Attack," AGARD CP-235, 1978.

25. Yechout, T.R., Introduction to Aircraft Flight Mechanics, Second Edition, AIAA, 2014.

26. Roskam, J., Airplane Flight Dynamics and Automatic Flight Controls, Pt. I., DAR Corporation, 1995.

27. Roskam, J., Airplane Flight Dynamics and Automatic Flight Controls, Pt. II., DAR Corporation, 1995.

28. F.S. Petersen; H.A. Rediess; J. Weil, “Lateral-Directional Control Characteristics Of The X-15 Airplane”, NASA TM X-726, NASA, 1962.

29. MIL-F-8785C, Military Specification: Flying Qualities of Piloted Airplanes, 1980.

30. MIL-STD-1797A, Flying Qualities of Piloted Aircraft, 1995.

31. Compton, H.R., Schiess, J.R., Suit, W.T, Scallion, W.I. and Hudgins, J.W., “Stability and Control Over the Supersonic and Hypersonic Speed Range,” NASA CP 2283 Part I, 1983.

32. Kirsten, P.W., Richardson, D.F. and Wilson, C.M., “Predicted and Flight Test Results of the Performance, Stability and Control of the Space Shuttle from Reentry to Landing,” NASA CP-2283 Vol. I, 1983.

33. Suit, W.T. and Scheiss, J.R., “Lateral and Longitudinal Stability and Control Parameters for the Space Shuttle Discovery as Determined from Flight Test Data,” NASA TM 100555, 1988.

34. Gamble, J., “The Application of Aerodynamic Uncertainties in the Design of the Entry Trajectory and Flight Control System of the Space Shuttle Orbiter,” NASA CP 2283 Part 1, 1983.

35. Bourne, C.A. and Kirsten, P.W., “Approach and Landing Characteristics of the Space Shuttle Orbiter,” NASA CP 2283 Part I, 1983.

36. Romere, P.O. and Whitnah, A.M., “Space Shuttle Entry Longitudinal Aerodynamic Comparisons of Flights 1-4 With Preflight Predictions,” NASA CP 2283 Part 1, 1983.

37. Miranda, L.R., Baker, R.D., and Elliot, W.M., “A Generalized Vortex Lattice Method for Subsonic and Supersonic Flow”, NASA CR 2875, 1977.

38. Souders, T.J. and Takahashi, T.T., “VORLAX 2020: Making a Potential Flow Solver Great Again,” AIAA 2021-2458, 2021.

39. Anon., “INVESTIGATION OF THE CHALLENGER ACCIDENT,” HR 99-1016, US Government Printing Office, 1986. Vol. 3, Appendix O. See: https://history.nasa.gov/rogersrep/v3o378b.htm

40. "Aircraft Rotations," https://www1.grc.nasa.gov/, 2023, See: https://www1.grc.nasa.gov/beginners-guide-to-aeronautics/aircraft-rotations/

41. Gamble, J.D., "The Development and Application of Aerodynamic Uncertainties: and Flight Test Verification for the Space Shuttle Orbiter", NASA - Johnson Space Center Houston, TX, February 21, 1985.

42. Freeman, D.C.Jr., Spencer, B.Jr., "Comparison of Space Shuttle Orbiter Low-Speed Static Stability and Control Derivatives Obtained from Wind-Tunnel and Approach and Landing Flight Tests," NASA Technical Paper 1779, 1980

43. Calloway, R.L., "Lateral-Directional Stability of the Space Shuttle Orbiter at Mach 6," NASA N84-10137,1983

44. Suit, W.T., Schiess, J.R., "Lateral and Longitudinal Stability and Control Parameters for the Space Shuttle Discovery as Determined from Flight Test Data," NASA TM 100555, 1988

45. "Space Shuttle Orbiter," https://nasa.fandom.com/, 2023, See: https://nasa.fandom.com/wiki/Space_Shuttle_orbiter

46. Anon. "Space Shuttle Atlantis STS-129 HD Landing, November 27, 2009, Runway 33, Kennedy Space Center". See: https://www.youtube.com/watch?v=5Qj3on0VTSs (accessed Nov. 7, 2022)

APPENDIX A

PLOTS FOR RECONSTRUCTED FLIGHT DATA

DATA COLLECTED AUGUST – MAY 2023

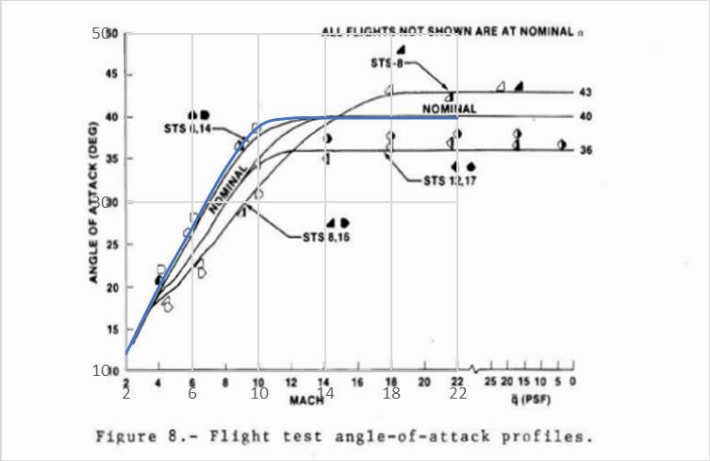

FIGURE 97. Flight Test Angle of Attack Schedule [17]

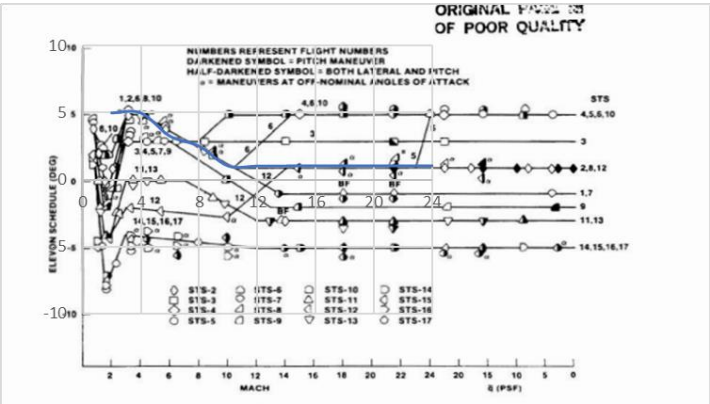

FIGURE 98. Flight Test Elevon Schedule [17]

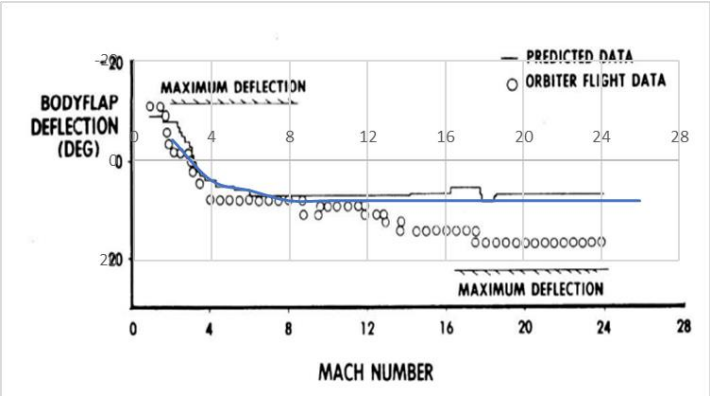

FIGURE 99. Flight Test Body Flap Schedule [32]

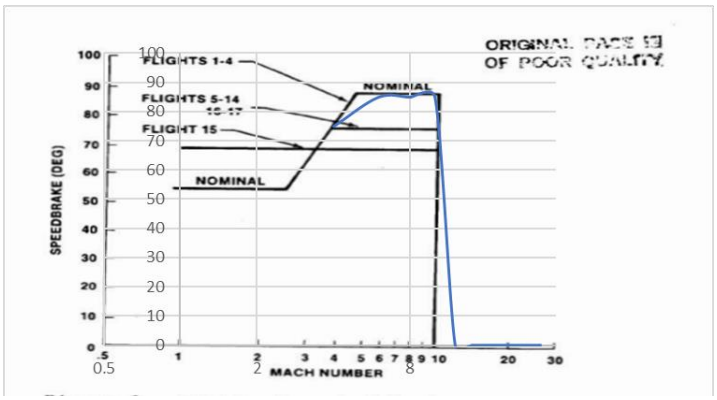

FIGURE 100. Flight Test Speed Brake Schedule [17]

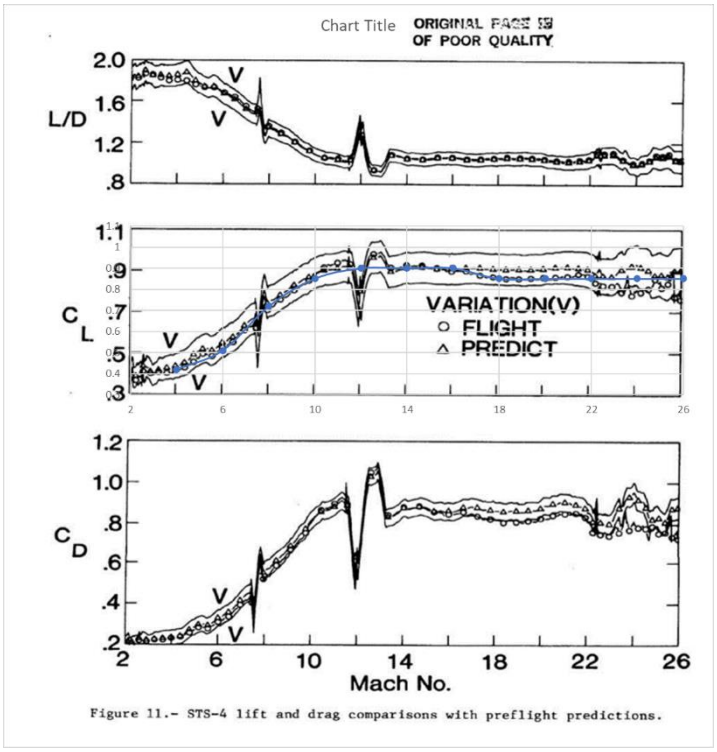

FIGURE 101. Flight Test L/D, CL, CD Schedule [31]

APPENDIX B

VORLAX INPUT FILE BASELINE SHUTTLE

Baseline_Orbiter_Neutral

```
*ISOLV    LAX      LAY      REXPAR    HAG      FLOATX    FLOATY
ITRMAX
 0        1        1        0.0       0        0         0           399
*NMACH    MACH
 1        0.3
*NALPHA   ALPHA
 10       -5. -2. 0. 2. 4. 6. 8. 10. 15. 20.
*LATRL    PSI      PITCHQ    ROLLQ     YAWQ      VINF
 1        -1       0         0         0         1
*NPAN     SREF     CBAR      XBAR      ZBAR      WSPAN
 10       2690.0   39.6      71.40     12.5      78.1
*
*
*-------------------------------------------------------------------------------
*000000001111111111222222222233333333334444444444555555555566666666667
7777777778
*234567890123456789012345678901234567890123456789012345678901234567890
1234567890
*
*Panel #1 Horizontal Body Panel
*X        Y        Z        CHORD
0        0        0        107.525
15.384   8.010    0        92.141
*NVOR     RNCV     SPC      PDL
4        50       0        0
*AINC1    ANINC2   ITS      NAP      IQUANT    ISYNT     NPP
0        0        0        0        2         0         0
*-------------------------------------------------------------------------------
*Panel #2 Vertical Body Panel
*X        Y        Z        CHORD
0        0        0        107.525
15.384   0        20.923   92.141
*NVOR     RNCV     SPC      PDL
6        50       0        0
*AINC1    ANINC2   ITS      NAP      IQUANT    ISYNT     NPP
0        0        0        0        1         0         0
*-------------------------------------------------------------------------------
*Panel #3 WING Glove
*X        Y        Z        CHORD
15.384   8.010    0        83.075
66.000   16.307   0        32.459
*NVOR     RNCV     SPC      PDL
20       35       0        0
```

```
*AINC1    ANINC2    ITS      NAP      IQUANT    ISYNT     NPP
0         0         0        0        2         0         0
*-------------------------------------------------------------------------------
*Panel #4 WING
*X        Y         Z        CHORD
66.0000   16.307    0        32.459
88.71     39.05     0        9.749
*NVOR     RNCV      SPC      PDL
20        20        0        0
*AINC1    ANINC2    ITS      NAP      IQUANT    ISYNT     NPP
0         0         0        0        2         0         0
*-------------------------------------------------------------------------------
*Panel #5 RIGHT Outboard Elevon
*X        Y         Z        CHORD
98.459    16.307    0        7.193
98.459    39.05     0        4
*NVOR     RNCV      SPC      PDL
20        10        0        0
*AINC1    ANINC2    ITS      NAP      IQUANT    ISYNT     NPP
0.        0.        0        0        1         0         0
*-------------------------------------------------------------------------------
*Panel #6 RIGHT Inboard Elevon
*X        Y         Z        CHORD
98.459    8.010     0        9.231
98.459    16.307    0        7.193
*NVOR     RNCV      SPC      PDL
20        10        0        0
*AINC1    ANINC2    ITS      NAP      IQUANT    ISYNT     NPP
0.        0.        0        0        1         0         0
*-------------------------------------------------------------------------------
*Panel #7 LEFT Outboard Elevon
*X        Y         Z        CHORD
98.459    -16.307   0        7.193
98.459    -39.05    0        4
*NVOR     RNCV      SPC      PDL
20        10        0        0
*AINC1    ANINC2    ITS      NAP      IQUANT    ISYNT     NPP
0.        0.        0        0        1         0         0
*-------------------------------------------------------------------------------
*Panel #8 LEFT Inboard Elevon
*X        Y         Z        CHORD
98.459    -8.010    0        9.231
98.459    -16.307   0        7.193
*NVOR     RNCV      SPC      PDL
20        10        0        0
```

```
*AINC1    ANINC2    ITS      NAP      IQUANT    ISYNT     NPP
0.        0.        0        0        1         0         0
*-------------------------------------------------------------------
*Panel #9 Air Brake
*X        Y         Z        CHORD
107.525   0         0        7
107.525   8.010     0        7
*NVOR     RNCV      SPC      PDL
20        10        0        0
*AINC1    ANINC2    ITS      NAP      IQUANT    ISYNT     NPP
0         0         0        0        2         0         0
*-------------------------------------------------------------------------------
*Panel #10 Vertical Stabilator
*X        Y         Z        CHORD
89.250    0         20.923   18.275
114.9     0         46.330   6.62
*NVOR     RNCV      SPC      PDL
20        10        0        0
*AINC1    ANINC2    ITS      NAP      IQUANT    ISYNT     NPP
0         0         0        0        1         0         0
*-------------------------------------------------------------------------------
* NXS     NYS       NZS
  00      00        00
```

APPENDIX C

VORLAX INPUT FILE 60-DEGREE WING TIP VERTICAL SHUTTLE

60DegWingTipVerticalShuttle

*ISOLV LAX LAY REXPAR HAG FLOATX FLOATY
ITRMAX
0 1 1 0.0 0 0 0 399
*NMACH MACH
10 0.5 0.7 0.8 0.9 1 2 3 4 5 6
*NALPHA ALPHA
10 -4 0 4 6 8 10 12 15 20 30
*LATRL PSI PITCHQ ROLLQ YAWQ VINF
0 -1 0 0 0 1
*NPAN SREF CBAR XBAR ZBAR WSPAN
11 3022.31 39.6 71.40 12.5 106.38
*
*---
*000000001111111111222222222233333333334444444444555555555566666666677777777778
*234567890123456789012345678901234567890123456789012345678901234567890123456789
0
*
*Panel #1 Horizontal Body Panel
*X Y Z CHORD
0 0 0 107.525
15.384 8.010 0 92.141
*NVOR RNCV SPC PDL
4 50 0 0
*AINC1 ANINC2 ITS NAP IQUANT ISYNT NPP
0 0 0 0 2 0 0
*---
*Panel #2 Vertical Body Panel
*X Y Z CHORD
0 0 0 107.525
15.384 0 20.923 92.141
*NVOR RNCV SPC PDL
6 50 0 0
*AINC1 ANINC2 ITS NAP IQUANT ISYNT NPP
0 0 0 0 1 0 0
*---
*Panel #3 WING Glove
*X Y Z CHORD
15.384 8.010 0 83.075
66.000 16.307 0 32.459
*NVOR RNCV SPC PDL
20 10 0 0
*AINC1 ANINC2 ITS NAP IQUANT ISYNT NPP

```
0       0       0       0       2       0       0
*-------------------------------------------------------------------------------
*Panel #4 WING
*X       Y       Z       CHORD
66.0000  16.307   0       32.459
88.71    39.05    0       9.749
*NVOR    RNCV     SPC     PDL
20       10       0       0
*AINC1   ANINC2   ITS     NAP     IQUANT   ISYNT    NPP
0        0        0       0       2        0        0
*-------------------------------------------------------------------------------
*Panel #5 RIGHT Outboard Elevon
*X       Y       Z       CHORD
98.459   39.05    0       4
98.459   16.307   0       7.193
*NVOR    RNCV     SPC     PDL
20       10       0       0
*AINC1   ANINC2   ITS     NAP     IQUANT   ISYNT    NPP
0        0        0       0       1        0        0
*-------------------------------------------------------------------------------
*Panel #6 RIGHT Inboard Elevon
*X       Y       Z       CHORD
98.459   16.307   0       7.193
98.459   8.010    0       9.231
*NVOR    RNCV     SPC     PDL
20       10       0       0
*AINC1   ANINC2   ITS     NAP     IQUANT   ISYNT    NPP
0        0        0       0       1        0        0
*-------------------------------------------------------------------------------
*Panel #7 LEFT Outboard Elevon
*X       Y       Z       CHORD
98.459   -39.05   0       4
98.459   -16.307  0       7.193
*NVOR    RNCV     SPC     PDL
20       10       0       0
*AINC1   ANINC2   ITS     NAP     IQUANT   ISYNT    NPP
0        0        0       0       1        0        0
*-------------------------------------------------------------------------------
*Panel #8 LEFT Inboard Elevon
*X       Y       Z       CHORD
98.459   -16.307  0       7.193
98.459   -8.010   0       9.231
*NVOR    RNCV     SPC     PDL
20       10       0       0
*AINC1   ANINC2   ITS     NAP     IQUANT   ISYNT    NPP
```

```
0       0       0       0       1       0       0
*-------------------------------------------------------------------
*Panel #9 Air Brake
*X       Y       Z       CHORD
107.525  0       0       7
107.525  8.010   0       7
*NVOR    RNCV    SPC     PDL
20       10      0       0
*AINC1   ANINC2  ITS     NAP     IQUANT  ISYNT   NPP
0        0       0       0       2       0       0
*-------------------------------------------------------------------------------
*Panel #10 Vertical Stabilator
*X       Y       Z       CHORD
89.250   0       20.923  18.275
114.9    0       46.330  6.62
*NVOR    RNCV    SPC     PDL
20       10      0       0
*AINC1   ANINC2  ITS     NAP     IQUANT  ISYNT   NPP
0        0       0       0       1       0       0
*-------------------------------------------------------------------------------
*Panel #11 Wing Outboard Cant
*X       Y       Z       CHORD
88.71    39.05   0       13.749
108.71   53.19   24.49   9.749
*NVOR    RNCV    SPC     PDL
20       10      0       0
*AINC1   ANINC2  ITS     NAP     IQUANT  ISYNT   NPP
0        0       0       0       2       0       0
*-------------------------------------------------------------------------------
* NXS    NYS     NZS
  00     00      00
```